Capability Assessment of Fully Polarimetric ALOS–PALSAR data for Discriminating Wet Snow from Other Scattering Types in Mountainous Regions

Gulab Singh, *Member, IEEE*, Gopalan Venkataraman, Yoshio Yamaguchi, *Fellow, IEEE*, and Sang-Eun Park, *Member, IEEE*

***Abstract*— This paper examines the capability assessment of fully polarimetric L-band data for the snow and nonsnow-area classifications. The data sets used are the fully polarimetric Advanced Land Observation Satellite–Phased Array-Type L-Band Synthetic Aperture Radar data, optical Advanced Land Observing Satellite (ALOS)–advanced visible and near-infrared radiometer-2 data close to the radar acquisition, and environmental satellite–advanced synthetic aperture radar data. Several parameters are used to discriminate the snow-covered areas from nonsnow-covered areas in the Indian Himalayan region, including backscattering coefficients, the ratio of cross/copolarized backscattering power and polarization fraction (PF) value. Supervised classification schemes are employed using polarimetric decomposition methods based on the complex Wishart classifier. The accuracy of the classification was found to be 97.95% for the Wishart-supervised classification. Among various parameters and methods, it was found that the alternative newly proposed PF scheme, based on the implementation of fully polarimetric synthetic aperture radar data, yielded the best classification result in the absence of the training samples. The PF value has been effective for discrimination of the snow-covered areas from nonsnow-covered areas, debris-covered glacier, and vegetation. The results of this investigation show that L-band fully polarimetric SAR data provide considerable improvement but may not possess the optimal capability to discriminate snow from other inherent natural and man-made scatterers in heavy snow-laden mountainous scenarios, which may require fully polarimetric S-band or C-band PolSAR measurements.**

***Index Terms*— Advanced Land Observing Satellite (ALOS)–PALSAR, glacier, H/A/$\bar{\alpha}$, Himalayas, polarization fraction, remote sensing, snow, wishart classifier.**

Manuscript received October 8, 2011; revised May 14, 2012, August 17, 2012, and November 11, 2012; accepted December 7, 2012. Date of publication May 2, 2013; date of current version December 12, 2013. This work was supported by the grant of Space Sensing, Ministry of Education, Japan, the JAXA-EORC for providing ALOS–PALSAR and ALOS–AVNIR-2 data free under Project JAXA-555, 599.

G. Singh, Y. Yamaguchi, and S.-E. Park are with the Graduate School of Science and Technology, Niigata University, Niigata 950-2181, Japan (e-mail: g.singh@wave.ie.niigata-u.ac.jp; yamaguch@ie.niigata-u.ac.jp; s.park@wave.ie.niigata-u.ac.jp).

G. Venkataraman is with the Centre of Studies in Resources Engineering, Indian Institute of Technology Bombay, Mumbai 400076, India (e-mail: gv@iitb.ac.in).

Color versions of one or more of the figures in this paper are available online at http://ieeexplore.ieee.org.

Digital Object Identifier 10.1109/TGRS.2013.2248369

I. Introduction

SNOW in mountainous areas such as the Himalayan region of India is especially sensitive to environmental changes due to their proximity to melting conditions at high altitudes and leads to hazards such as avalanches and sudden water runoff. Snow avalanches cause severe damages in populated mountainous regions, and sudden water-releases do flood out the entire valley villages. An intrinsic relationship exists between snow and its discharge in the emanating river system. The snow cover serves as a temporal intermediate storage containment, releasing ecologically and economically important meltwater during warm periods. Timely information about snow parameters and their temporal and spatial variability are essential factors in climatology, local weather and avalanche forecasting, and for the hydropower production in high mountainous areas. Due to strong spatial and time-dependent dynamics of the snow cover, frequent observations over large regions are necessary.

For snow-covered areas within the Indian Himalayan region, data collection by conventional manual and ground-based sensor methods is difficult, both in terms of logistic problems and sporadic occurrences. Even when available, such snow-cover data may not be representative of a large area due to the limited point measurements and are not practical for large mountainous regions covering many mountains, valleys, and topographies. Satellite remote sensing is in need, and offers great potential in this paper of dynamically changing environments related to the high altitude cold regions mainly because of its repetitive capability and synoptic coverage. The changing snow-cover has unique reflectance characteristics in different spectral bands of optical sensors, which may provide information on physical properties as well as on the areal extent of the snow cover under cloud-free conditions. However, there exist some difficulties in rugged high mountainous areas, such as an effect of varying solar illumination due to topography, shadow and cloud-cover, etc., on the spectral response of snow. Synthetic aperture radar (SAR) imaging using microwave sensors is an alternative and the most important techniques for collecting data over high mountainous regions. Microwaves can penetrate clouds

and fog, rain, and moist precipitation, and provide an all-weather observational capacity, independent of time and solar illumination; however, great care must be taken in choosing the proper frequency band for specific applications, and the most desirable SAR sensors of optimal bands such as the S-band may not yet be available. Furthermore, it is essential that polarimetric synthetic aperture radar (PolSAR) sensors are implemented for complete characterization of the pertinent parameters for discriminating snow-covered areas from uncovered areas at all of the pertinent microwave bands. Therefore, this paper makes use primarily of the existing fully polarimetric Advanced Land Observation Satellite–Phased Array-Type L-Band Synthetic Aperture Radar (ALOS–PALSAR) L-band sensor with some reference to the fully polarimetric TerraSAR-X and RADARSAT-2, for which comparative data sets were not available for this region. It is understood that the microwave backscattering from the natural snow-cover is the sum of surface scattering at the air/snow interface, volume scattering within the snowpack, scattering at the snow/ground interface, and heterogeneous volumetric scattering from the underlying surface (if applicable) [1]–[3]. For the case of dry snow with wetness less than 1%, the backscattering is small because snow behaves as dielectric material with varying dielectric constants $1.2 \sim 2.0$. The volume scattering is governed by a mixture of dielectric properties of ice crystals and air within the snow and its density [2]. The volume scattering increases with the snow grain size, inter-layering, and the amount of inherent snow. Snow state is a dynamic process as a function of time, and influences the SAR backscatter because older snow has larger grain sizes than the new snow grains. For the case of wet snow with wetness larger than 1%, the situation becomes totally different [1], [4]–[7]. When the top layer becomes wet (4%–5% wetness by volume), the backscattering is reduced [6]. Mätzler and Schanda [6] reported that the backscattering coefficients for C-band like-polarization (horizontal–horizontal HH and vertical–vertical VV) at a look angle 40° from the wet snow were 10 times lower than those from the dry snow and that the cross-polarized backscattering coefficient was 100 times lower. The attenuation constant inside snow is proportional to frequency. At snow wetness of 3% and density of 0.4 g/cm^3, the theoretical attenuation constant becomes 17.4 dB/m for 3 GHz (S-band) and 100 dB/m for 10 GHz (X-band) [7]. The relationship between scattering mechanism and snow wetness has been discussed by Shi *et. al.* [8]. The increase of liquid water in snow causes a larger reflection at the air/snow interface and a significant increase of the absorption coefficient within the snowpack. The surface scattering from the snow cover is proportional to the wetness, and the volume scattering is inversely correlated to the snow wetness [9].

Various methods have been presented for the wet snow-cover mapping using multitemporal single-polarization channel C-band SAR data [10]–[14]. However, it has been found that they are not sufficient for detecting the snow-over accumulation areas of glaciers, because of poor information at a single frequency with a fixed polarization [15]–[17]. It is necessary to increase information on the snow-cover mapping using multifrequency- and/or multipolarization sensor implementation.

Based on the ratio technique [10], the snow-cover mapping studies were carried out using multitemporal- and multifrequency SAR [15] sensors. It was found that TerraSAR-X provided very good information about the snow-extent. In other words, X-band (9.6 GHz) repeat-pass SAR data with single polarization showed a promising capability for discriminating snow from other pertinent scattering objects at flat terrain as compared to L- and C-band SAR data with single polarization. This indicates that the discrimination of the snow-cover, using intermediate and low-frequency SAR data with single polarization, is not appropriate [15].

The PolSAR data do contain more information than the single- or dual-polarization SAR data. Fully polarimetric data provide the only capability for optimization of the polarimetric contrast and other polarimetric parameters, which are useful and essential for accurate discrimination between the snow-covered areas and nonsnow-covered areas [16], [17]. PolSAR data analysis can hence be extremely useful to develop methodology for discriminating snow from other surface features. Moreover, understanding and retrieving information from polarimetric SAR signatures of snow-covered terrain surfaces have become a crucial issue in the field of the SAR remote-sensing applications.

There is a need to explore the potential of PolSAR data, incorporating the knowledge of polarimetric microwave interactions with scattering objects and a methodology for retrieval of snow parameters (e.g., wetness, density, grain size, depth) and to discriminate the snow-cover from other natural or man-made scatterers. Since there is no proven methodology/algorithm available hitherto, the main scope of this paper is to assess the capability of fully polarimetric L-band ALOS–PALSAR data for snow discrimination from other scattering scenarios in the Indian Himalayan regions—also because we had access only to the L-band ALOS–PALSAR data sets. In this paper, we examined backscattering coefficients, the ratio of cross/copolarized backscattering power, the polarization fraction (PF) value, and the supervised classification scheme using the polarimetric decomposition method based on the complex Wishart classifiers, which all require fully polarimetric PolSAR data sets. It is shown that the PF value is effective for assessing the capability of ALOS–PALSAR data for the snow discrimination. Furthermore, a new PF-based method is introduced and proposed in this investigation.

Yet, it needs to be emphasized that neither the L-band, C-band nor X-band PolSAR sensor data are optimal, and we are waiting desperately for being made available a fully polarimetric S-Band PolSAR satellite-sensor system, which is in need also for a plethora of other related applications in environmental and geophysical remote sensing of the terrestrial surface covers.

II. Test Site and Data Used

A. Test Site

Due to the limited availability of fully polarimetric ALOS–PALSAR data, this paper is confined to the Gangotri–

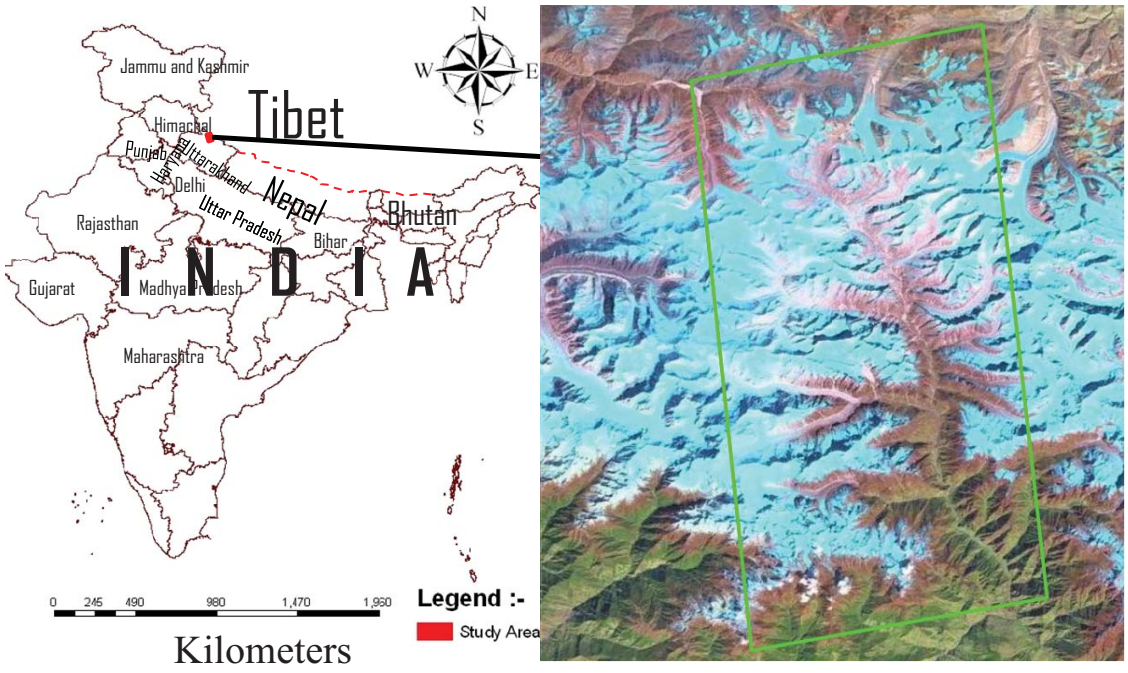

Fig. 1. Location of the test sites within the Indian Himalayan region.

TABLE IA
ENVISAT–ASAR APS AND ALOS–PALSAR SLC DATA

Date	Sensor	Polarization	Off-Nadir Angle(0)	Orbit Pass	GMT (hh:mm:ss)	Region
19/05/2007	ENVISAT–ASAR	HH + VV	39.1–42.8	Descending	04:35:58	Badrinath
10/11/2007	ENVISAT–ASAR	HH + VV	39.1–42.8	Descending	04:37:42	Badrinath
12/05/2007	ALOS–PALSAR	Quad-Pol	21.5	Ascending	17:04:40	Badrinath
12/11/2007	ALOS–PALSAR	Quad-Pol	21.5	Ascending	17:04:31	Badrinath
06/06/2010	ALOS–PALSAR	Quad-Pol	21.5	Ascending	17:07:20	Gangotri
26/05/2009	ALOS–PALSAR	Quad-Pol	21.5	Ascending	21:38:15	Agassiz Horn

In Table IA, Quad-Pol represents the combinations of four polarization returns HH, HV, VH, VV, and GMT stands for the Greenwich Mean Time.

TABLE IB
MULTISPECTRAL (MS) DATA OF ALOS–AVNIR-2

Date	Level	Orbit Pass	Channel	Look Angle	Cloud Cover	Area
06-05-2007	1B2	Descending	MS	Nadir	21%–30%	Gangotri–Badrinath
24-05-2010	1B2	Descending	MS	Nadir	$<2\%$	Gangotri–Badrinath
24-05-2009	1B2	Descending	MS	Nadir	$<2\%$	Agassiz Horn

Badrinath region of the Indian Himalayas (Fig. 1). This region is used as a test site for an extensively snow-covered region having many glaciers of varying dimensions that act as huge freshwater reservoirs. The test site covers Gangotri, Panpatia, Satopanth, Bhagirath Kharak, and Suraji Bank glaciers. Numerous small-sized glaciers and snow-covered areas also occur within the neighborhood. The region falls between latitude 30°30' N and 31°15' N and longitude between 79°15' E and 79°30' E.

B. Satellite Data

In this paper, the fully polarimetric L-band ALOS–PALSAR single-look complex (SLC) level 1.1 data and partial polarimetric C-band ENVISAT–ASAR data in alternating polarization single-look complex (APS) mode with HH and VV combination of polarization are used for the snow classification over the Badrinath area in the test site. Moreover, ALOS–AVNIR-2 data is used to interpret snow-covered and nonsnow-covered areas, and to select the training sample for supervised classification. In addition, for verification, one-day difference images of ALOS–PALSAR and AVNIR-2 are used over the Agassiz Horn mountainous region in the Bernese Alps of Switzerland to assess the ALOS–PALSAR capability with the newly proposed PF method. Lists of ALOS–PALSAR, ENVISAT–ASAR, and ALOS–AVINIR-2 data are shown in Table I.

TABLE II
FEW LOCATIONS FIELD CONDITION DURING ALOS PASSES

Date	Maximum Temperature (°C)	Minimum Temperature (°C)	Sunshine (hrs)	Snow Depth (cm)	Location	Type of Station	Station Altitude (m)
12-05-2007	19.9	1.5	0745	0	Bhojbasa	Observatory	3800
12-05-2007	1.5	−2.8	-	0	Nandanvan	AWS-1	4450
12-05-2007	−2.5	−7.5	-	269	Kalindikhal	AWS-2	5900
12-11-2007	7.8	−4.4	-	0	Bhojbasa	Observatory	3800
12-11-2007	−6.6	−13.1	-	221	Kalindikhal	AWS-2	5900
24-05-2010	19.5	1.5	0930	0	Bhojbasa	Observatory	3800
06-06-2010	17	0	0730	0	Bhojbasa	Observatory	3800

C. Field Data and Weather Condition

In general, snow-cover areas become wet in May (early summer) over the Indian Himalayan snow-bound region, with significant melting [18], [19] taking place. The magnitude of the backscatter depends on the snow density and water content, and the depth of the snowpack [19]. The snowpack is also heterogeneous with the snow-grain particles being compressed during winter season and possessing high density due to the snow accumulation and the alternating melting cycle [18]. Since the snowpacks on May 12, 2007 and May 06, 2010 are wet due to the beginning of snow melting, the snowpacks contain water and are not so transparent at the L-band frequency. Limited data were available from a nearby manual observatory as well as from automated weather stations (AWS), which are shown in Table II. The locations of the observatory and automated weather stations AWS-1 and AWS-2 are shown by red dot in Fig. 2.

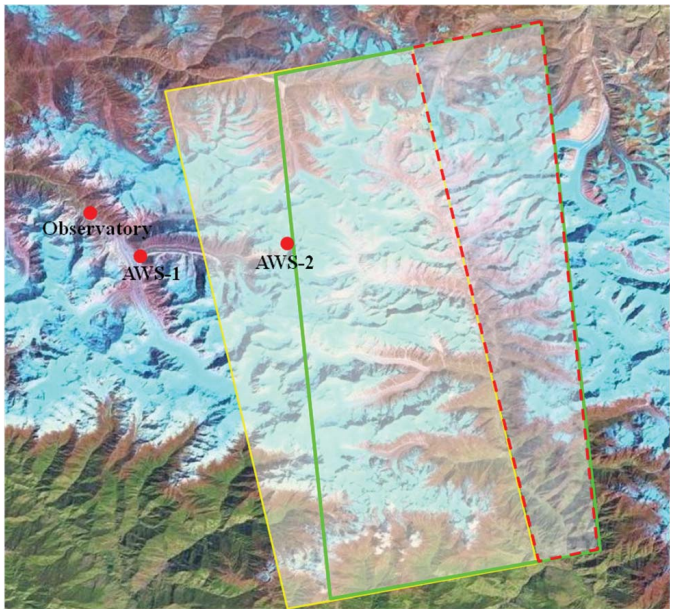

Fig. 2. Locations of the observatory and automated weather stations AWS-1 and AWS-2 are shown by red dots. Yellow quadrilateral shows the sensor ephemeris parameter footprint, green quadrilateral shows the acquired ALOS–PALSAR scene of May 12, 2007, and the dashed red quadrilateral shows offset area between them.

III. METHODS AND TECHNIQUES USED

This section explains the SAR data processing and methods for snow discrimination. The methodology for the PolSAR data analysis of the snow-covered areas and polarimetric descriptors are explained for the snow-cover mapping and snow discrimination from other natural and man-made scattering scenarios.

A. SAR Data Preprocessing

1) Sigma Naught σ^0 Calculations:

a) ENVISAT–ASAR: We have converted ENVISAT–ASAR (dual polarized SLC data) digital number values into backscattering coefficients (power value). The ENVISAT–ASAR alternating-polarized SLC (APS) data of 19 May and 10 November, 2007 have been processed. All Images were multilooked 5 times in azimuth and 1 time in the range direction. All the images were subjected to speckle suppression using the Frost filter [20] with window size 5 × 5, coefficient of variation and smoothing parameter. Data processing of dual polarization ENVISAT–ASAR data is explained in [18] and [19] including radiometric correction of the SAR backscatter for inverting the snow wetness. However, radiometric corrections of the backscattering coefficient (σ^0) images are not made here, because Rott and Nagler [21] found that the requirements for correction of the local incident angle were relaxed when multitemporal SAR data were used in the ratio method. In this paper, coregistration of the SAR images is done for snow mapping by implementation of the Nagler [10] algorithm.

b) ALOS–PALSAR: The backscattering coefficient (σ^0) from ALOS–PALSAR level 1.1 products can be calculated using the following equation given by JAXA [22]

$$\sigma^0 = 10\log_{10}\left(I^2 + Q^2\right) + CF - 32 \tag{1}$$

where the calibration factor (CF) = −86 dB and I and Q are in-phase and quadrature components of a pixel.

Initially, the data were multilooked one time in the range and six times in azimuth so that the spatial resolution can be reduced to 23 × 21 m (range × azimuth). The sigma naught images were Frost-filtered [20] with window size of 5 × 5 before the snow mapping, based on the ratio method.

2) Coherency Matrix Calculation: The calibrated complex 2 × 2 backscattering matrix **S** of ALOS–PALSAR in

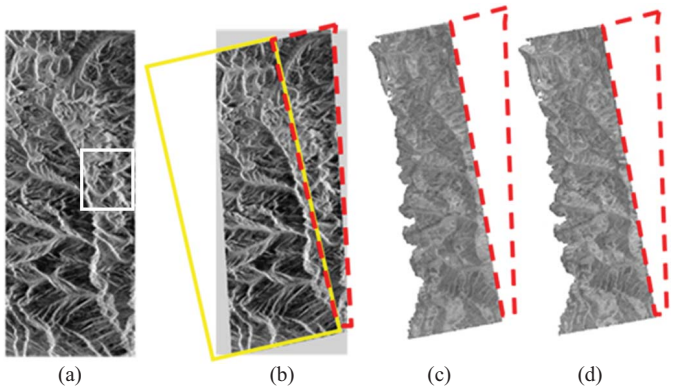

Fig. 3. VV-Polarized ALOS–PALSAR image of May 12, 2007. (a) Without georectification. (b) 2-D georectification. (c) 3-D georectification (orthorectified). (d) Local incident angle correction (reddashed quadrilateral is showing the areas reduction in orthorectified image size).

horizontal–vertical $H-V$ basis is expressed as

$$\mathbf{S} = K \begin{bmatrix} S_{\mathrm{HH}} & S_{\mathrm{HV}} \\ S_{\mathrm{VH}} & S_{\mathrm{VV}} \end{bmatrix} \tag{2}$$

where $K = 10^{(CF-32)/10}$, and the elements of scattering matrix S_{HH}, S_{VV}, and S_{HV} are called complex backscattering coefficients [22]. The elements S_{HH} and S_{VV} produce the power return in the copolarized channel and the elements S_{HV} and S_{VH} produce the power in the cross-polarization channels. $S_{\mathrm{HV}} = S_{\mathrm{VH}}$ is here assumed for the backscattering case.

The scattering matrix $\boldsymbol{S}$ can be converted to the coherency matrix with multilook factor 6 × 1 (azimuth × range). The measured coherency matrix for fully polarimetric ALOS–PALSAR data is written in (3), shown at the bottom of the page.

Before performing decomposition and implementing the Wishart-supervised classifier on the coherency matrix, the refined Lee filter with window size 5 × 5 is applied for reducing the speckle noise [23].

B. Postprocessing: Georectification

A slant range to the ground-range conversion is made before georectification. However, in highly rugged mountainous regions, SAR images with 2-D georectification do not match-fit optical images accurately [24]. There is a requirement of 3-D georectification, which is also known as orthorectification [19], [25]. Orthorectification reduces both the area of interest in images and its image quality. The offset between the sensor ephemeris parameters and the acquired scene reduces the image size (Figs. 2 and 3). The pixel resampling during the process of 2-D or 3-D georectification reduces the image quality (Fig. 3). To preserve the area of interest and image quality requirements, it has been decided to perform georectification after the image classification and snow-cover mapping with the implementation of newly proposed and existing algorithms. However, radiometric correction for image classification is not made here due to the low resolution of the employed digital elevation model (90 m), which provides little help in high-relief regions [26]. Even unidentified or else layover areas due to steep slopes are taken as a special class to extract terrain influences in supervised classified images.

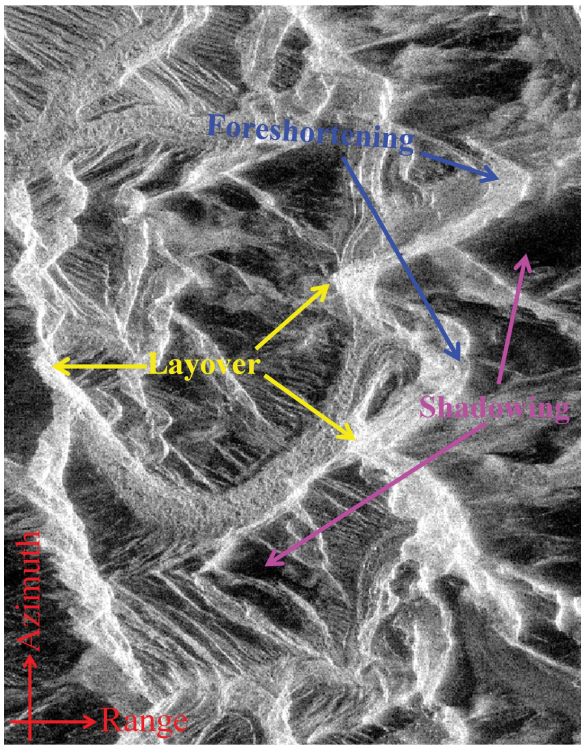

Fig. 4. Examples of layover, foreshortening, and shadowing in the white box on Fig. 3(a).

In addition, 3-D georectification is made after a snow detection for comparing the results of the newly proposed method with optical data results in Section V. Moreover, measurements of polarization properties and ratio between two or more PolSAR-derived parameters can be used without radiometric calibration [19], [27], [28]. Because these measurements are derived from the ratio of two or more measurements at the same pixel, the radiometric error that topography causes cancels except in areas of the radar shadowing and layover (Fig. 4). To suppress the distorted (layover and shadowing) areas in the final snow map of the proposed method, several eigenvalue-based derived parameters are analyzed.

C. Snow-Cover Discrimination Methods

1) Single-Polarization and Multipolarization Repeat-Pass Method: The principle behind the snow cover mapping is based on the reduced backscattering coefficient from the snow-covered surface as compared to nonsnow-covered surfaces.

$$\langle [\mathbf{T}] \rangle = \frac{1}{2} \begin{bmatrix} \langle |S_{\mathrm{HH}} - S_{\mathrm{VV}}|^2 \rangle & \langle (S_{\mathrm{HH}} + S_{\mathrm{VV}})(S_{\mathrm{HH}} - S_{\mathrm{VV}})^* \rangle & 2\langle (S_{\mathrm{HH}} + S_{\mathrm{VV}}) S_{\mathrm{HV}}^* \rangle \\ \langle (S_{\mathrm{HH}} - S_{\mathrm{VV}})(S_{\mathrm{HH}} + S_{\mathrm{VV}})^* \rangle & \langle |S_{\mathrm{HH}} - S_{\mathrm{VV}}|^2 \rangle & 2\langle (S_{\mathrm{HH}} - S_{\mathrm{VV}}) S_{\mathrm{HV}}^* \rangle \\ 2\langle S_{\mathrm{HV}}(S_{\mathrm{HH}} + S_{\mathrm{VV}})^* \rangle & 2\langle S_{\mathrm{HV}}(S_{\mathrm{HH}} - S_{\mathrm{VV}})^* \rangle & 4\langle |S_{\mathrm{HV}}|^2 \rangle \end{bmatrix} \tag{3}$$

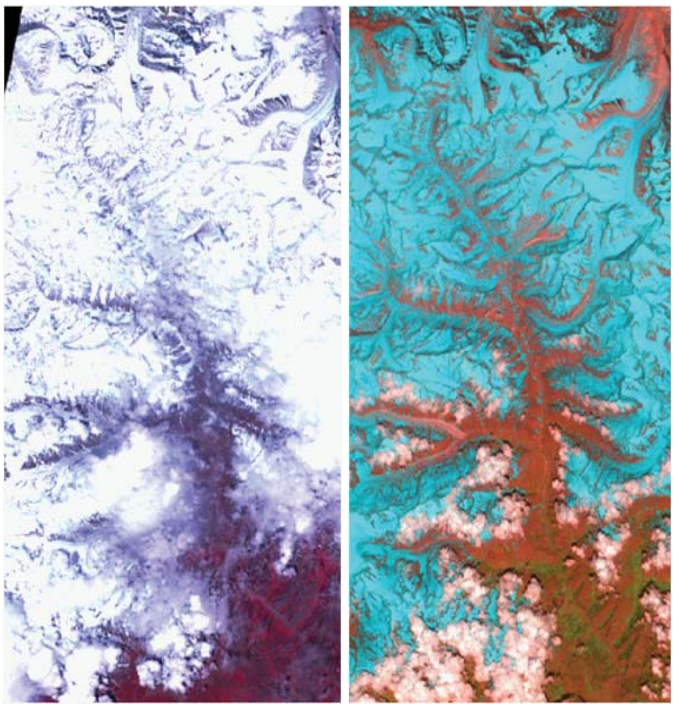

(a) (b)

Fig. 5. (a) ALOS–AVNIR-2 FCC image of 06-05-2007. (b) IRS-P6-AWiFS FCC image of 10-05-2007.

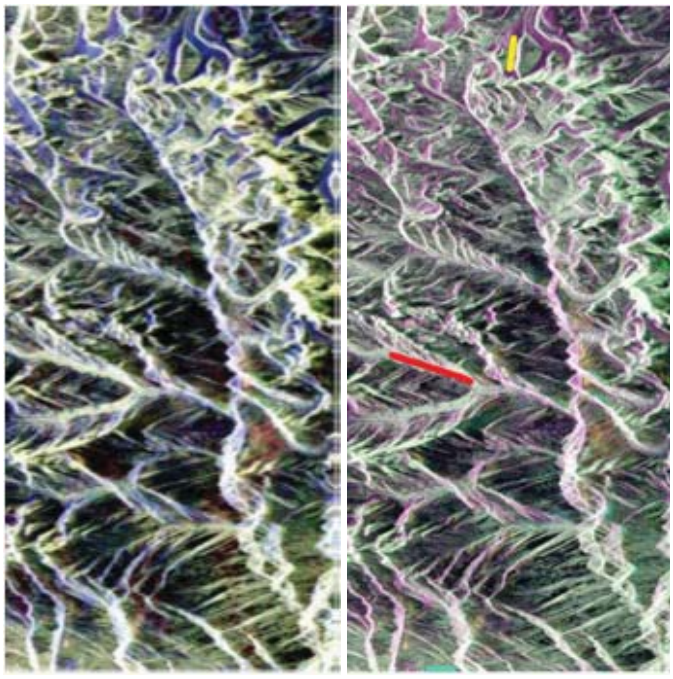

(a) (b)

Fig. 6. (a) Pauli RGB of 06-05-2007. (b) ALOS–PALSAR σ^0 color combination image of 06-05-2007. HH (Red) - HV (Green) - VV (Blue).

For snow mapping, the Nagler [10] algorithm has been applied. In this change-detection algorithm, the ratio between the backscattering coefficient within the melting period and a snow-free reference image is taken. An appropriate threshold value based on ASAR data is used to delineate snow from other surfaces [12].

2) Multipolarization Single-Pass Method for Snow-Cover Discrimination: In this paper, the following condition has been applied for mapping the snow cover:

$$\frac{\sigma^0_{pq}}{\sigma^0_{pp}} < m \quad \text{snow} \tag{4}$$

where $m = 0.2$ is used and an explanation of this selection is given under Section IV-D of this paper. σ^0_{pq} is the backscattering coefficient of cross-polarization, and σ^0_{pp} is the backscattering coefficient of the copolarization data at L-band. Shi *et al.* [27] also used a similar procedure for C-band data and their results are in agreement with those of Rott *et al.* [29].

D. Decomposition Models

SAR polarimetry is important for the snow studies and for discriminating snow from nonsnow-cover. In this paper, for the examination of the capability of L-band PALSAR polarimetric data for discriminating snow from other natural and man-made scatterers and also for classifying PALSAR data, existing decomposition models have been applied. Since most of the scattering occurring in our test site is natural, the incoherent decomposition theories derived from the coherency matrix have been implemented because of the mixed scattering behavior.

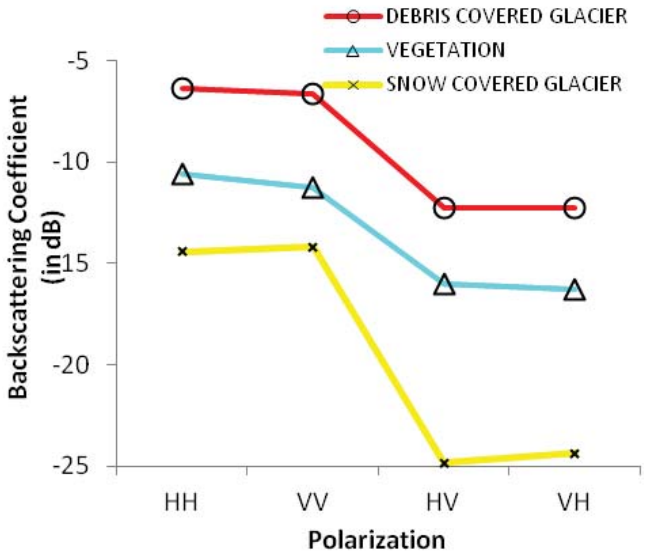

Fig. 7. Backscattering coefficient (σ^0) comparison of quad polarization ALOS–PALSAR for various scattering scenarios (profiles for Debris covered glacier, vegetation and snow covered glacier are in red, cyan and yellow in Fig. 6(b) respectively)

E. $H/A/\bar{\alpha}$ Decomposition

The $H/A/\bar{\alpha}$ decomposition technique [30] is based on three eigenvalues (λ_1, λ_2, and λ_3 with decreasing magnitude) of the coherency matrix $\langle[T]\rangle$, and defines the entropy H, the anisotropy A, and the angle $\bar{\alpha}$. This method does not depend on the assumption of a particular underlying statistical distribution, and it is free from the physical constraints imposed by such multivariate models.

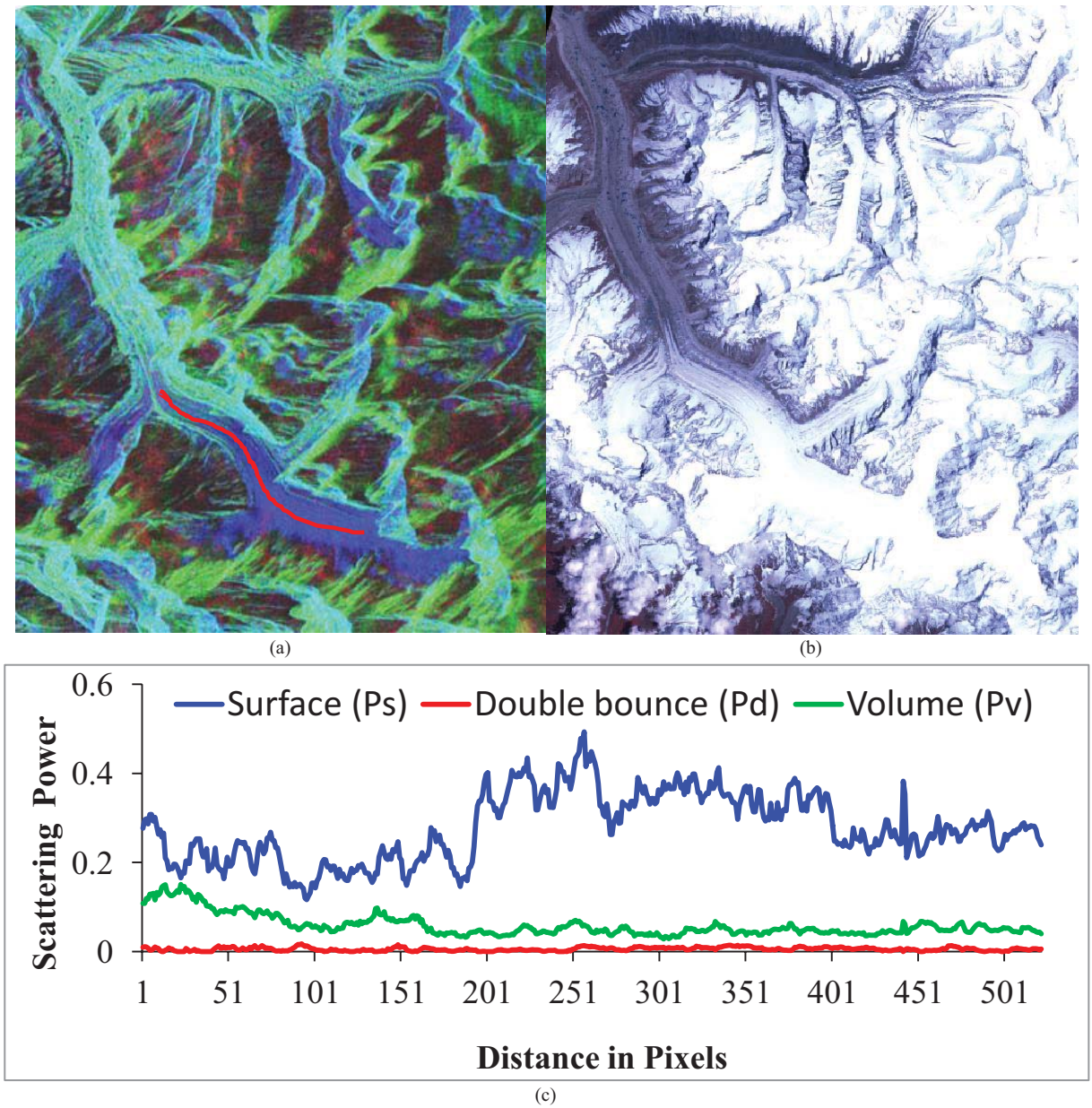

Fig. 8. (a) Four-component-scattering decomposition FCC of 06-06-2010 over Gangotri glacier [Red: double-bounce scattering, Green: volume-scattering, Blue: surface-scattering]. (b) ALOS–AVNIR-2 FCC image of 25-05-2010 over Gangotri glacier. (c) Scattering power profile over snow covered Gangotri glacier.

The entropy (H) can be defined from the eigenvalues of $[T]$

$$H = -P_1 \log_3 P_1 - P_2 \log_3 P_2 - P_3 \log_3 P_3 \quad (5)$$

$$0 \leq P_i = \frac{\lambda_i}{\sum_{i=1}^{3} \lambda_i} \leq 1 \quad (6)$$

where P_i is pseudo probability, which can be obtained from the eigenvalue λ_i.

The entropy indicates depolarization of the scattering ensemble. If entropy is low ($H < 0.3$), then scatterers are weakly depolarized, when entropy is high, then scattering is highly depolarized.

The polarimetric anisotropy A is the linear combination ratio of the second and third eigenvalues of $[T]$. The anisotropy can be defined as

$$A = \frac{\lambda_2 - \lambda_3}{\lambda_2 + \lambda_3}; \quad 0 \leq A \leq 1. \quad (7)$$

The polarimetric anisotropy A is a complementary parameter of the polarimetric entropy H. Anisotropy measures the relative importance of the second and the third eigenvalues of coherency matrix. From an application point of view, the anisotropy A can be applied as a means of discrimination when entropy $H > 0.7$.

The mean scattering ($\bar{\alpha}$) angle is defined in (8) and it varies from 0° to 90°

$$\bar{\alpha} = P_1\alpha_1 + P_2\alpha_2 + P_3\alpha_3. \quad (8)$$

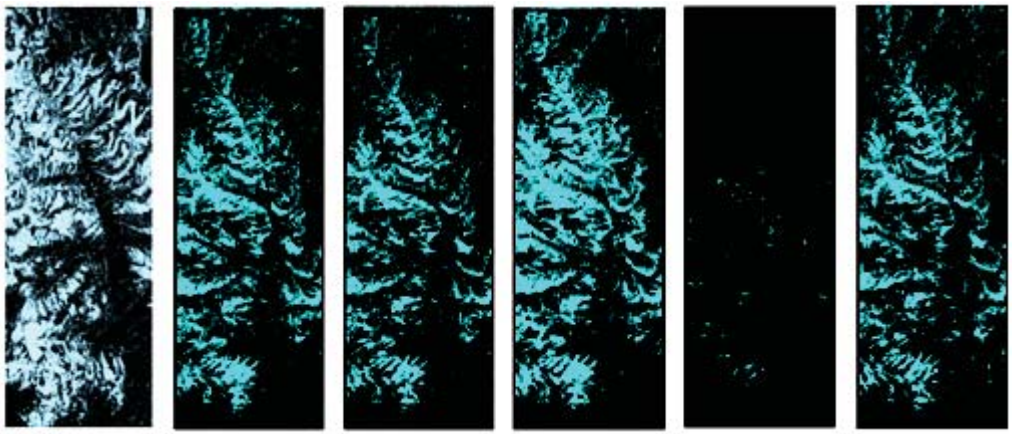

Fig. 9. Snow-cover maps using repeat-pass SAR data (a) ENVISAT–ASAR VV-polarization and (b)–(f) PALSAR (**cyan** color: snow, **black** color: snow-free).

TABLE III
ACCURACY OF SNOW AND NONSNOW DISCRIMINATION FOR ALOS–PALSAR DATA BASED ON TEMPORAL CHANGE TECHNIQUE

User-Defined Sample	Classified Sample							
	Snow-Free (%)				Snow (%)			
	VV/VV	HH/HH	HV/HV	HH/VV	VV/VV	HH/HH	HV/HV	HH/VV
Snow-Free	72.67	82.59	64.57	76.32	27.33	17.41	35.43	23.68
Snow	71.43	74.61	56.75	75.23	28.57	25.39	43.25	24.77
Overall Accuracy = 40.8% (VV), 41.25% (HH), 49.16% (HV), 39.06% (HH/VV)								

F. Yamaguchi Four-Component Scattering Power Decomposition

Based on the physical scattering mechanisms, the four-component scattering power decomposition method has been presented in [31] and [32]. According to this decomposition theorem, the coherency matrix can be expanded into 4 sub-matrices as

$$\langle [T] \rangle = f_s \langle [T] \rangle_{\text{surface}} + f_d \langle [T] \rangle_{\text{double}} + f_v \langle [T] \rangle_{\text{vol}} + f_c \langle [T] \rangle_{\text{helix}} \quad (9)$$

where $f_s, f_d, f_v,$ and f_c are surface-, double bounce-, volume-, and helix-scattering coefficients, respectively. It is possible to determine the corresponding 4-scattering powers from these coefficients. $\langle [T] \rangle_{\text{surface}}$, $\langle [T] \rangle_{\text{double}}$, $\langle [T] \rangle_{\text{vol}}$, and $\langle [T] \rangle_{\text{helix}}$ are surface-, double bounce-, volume-, and helix-coherency matrices, respectively [31], [32].

G. Polarization Fraction

The maximum receiving power ($P_{\max}$) and the minimum power ($P_{\min}$) can be obtained in the copolarization or the cross-polarization radar channels, respectively, when fully polarimetric scattering matrix measurements are available and used.

The PF is defined from $P_{\max}$ and $P_{\min}$, which gives van Zyl's polarization purity of return signal [33]

$$\text{van Zyl's PF} = \frac{P_{\max} - P_{\min}}{P_{\max} + P_{\min}}. \quad (10)$$

The PF can also be calculated based on eigenvalue [34]

$$\text{PF} = 1 - \frac{3\lambda_3}{\lambda_1 + \lambda_2 + \lambda_3} = 1 - 3P_3; \quad 0 \leq \text{PF} \leq 1 \quad (11)$$

where λ_1, λ_2, and λ_3 are the eigenvalues of coherency matrix.

H. Other Polarimetric Parameters

1) Polarimetric Asymmetry (PA): is defined as [34]

$$\text{PA} = \frac{P_1 - P_2}{\text{PF}}. \quad (12)$$

2) Lüneburg Anisotropy (LA): has been introduced in [35] and is defined as

$$LA = \sqrt{\frac{3}{2}} \sqrt{\frac{\lambda_2^2 + \lambda_3^2}{\lambda_1^2 + \lambda_2^2 + \lambda_3^2}}; \quad 0 \leq LA \leq 1. \quad (13)$$

3) SERD and DERD: Allain *et al.* [36] derived two alternative eigenvalue-based parameters namely the single-bounce eigenvalue relative difference (SERD) and the double-bounce eigenvalue relative difference (DERD) to characterize natural scattering media. These two parameters are derived from the coherency matrix $\langle [T] \rangle$ under the reflection symmetry condition [23]. SERD and DERD are deified as

$$\text{SERD} = \frac{\lambda_S - \lambda_3'}{\lambda_S + \lambda_3'} \quad \text{and} \quad \text{DERD} = \frac{\lambda_D - \lambda_3'}{\lambda_D + \lambda_3'} \quad (14)$$

where λ_S and λ_D are the two eigenvalues for the single-bounce- and for the double-bounce scattering mechanisms

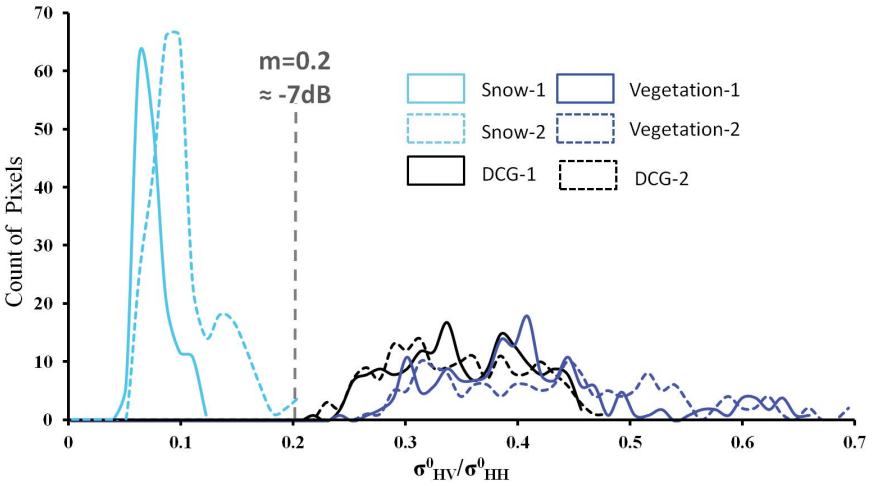

Fig. 10. Histograms for threshold selection between snow-covered and other mountainous regions.

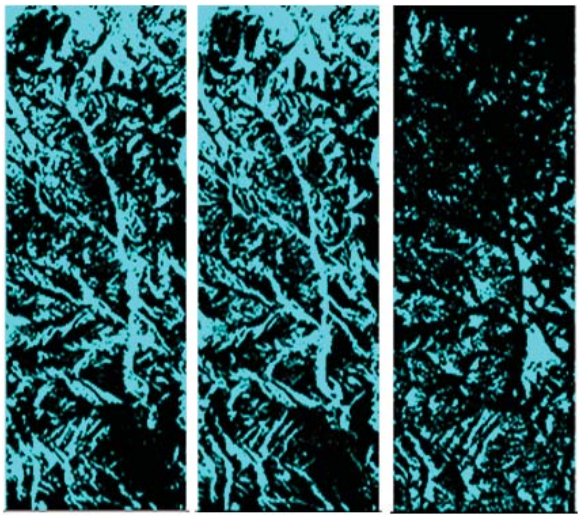

Fig. 11. Snow-cover maps using single-pass PALSAR data (**cyan** color: snow, **black** color: snow-free). (a) HV/HH. (b) VH/VV. (c) HH/VV.

respectively. λ_S and λ_D are fixed by using the following condition:

$$\text{if } \alpha_1 \le \frac{\pi}{4} \quad \text{or} \quad \alpha_2 \ge \frac{\pi}{4} \quad \Rightarrow \begin{cases} \lambda_S = \lambda_1' \\ \lambda_D = \lambda_2' \end{cases}$$
$$\text{if } \alpha_1 \ge \frac{\pi}{4} \quad \text{or} \quad \alpha_2 \le \frac{\pi}{4} \quad \Rightarrow \begin{cases} \lambda_S = \lambda_2' \\ \lambda_D = \lambda_1'. \end{cases} \tag{15}$$

In (14) and (15), λ_1', λ_2', and λ_3' are the first, second and third eigenvalues of the coherency matrix subject to the reflection symmetry condition.

4) Copolarization Coherence: The coherence between the two copolarized radar channels is given in terms of scattering matrix [23]

$$\gamma = \frac{\langle S_{HH} S_{VV}^* \rangle}{\sqrt{|S_{HH}|^2 \, |S_{VV}|^2}}. \tag{16}$$

5) PPD: The polarimetric copolarization phase difference (PPD) between the two copolarized channels in polarimetric radar is the phase angle of the copolarized correlation coefficient. The PPD ($\Delta\phi$) can be estimated from the following relationship [23]

$$\Delta\phi = \tan^{-1}\left(\frac{\text{Im}\langle S_{HH} S_{VV}^* \rangle}{\text{Re}\langle S_{HH} S_{VV}^* \rangle}\right). \tag{17}$$

TABLE IV
ACCURACY OF SNOW AND NONSNOW DISCRIMINATION BASED ON HV/HH AND VH/VV RATIO

User-Defined Sample	Classified Sample			
	Snow-Free (%)		Snow (%)	
	HV/HH	VH/VV	HV/HH	VH/VV
Snow-Free	64.70	67.57	35.30	32.43
Snow	3.62	4.17	96.38	95.83
Overall Accuracy = 74.40% (HV/HH), 74.46% (VH/VV)				

IV. RESULTS AND DISCUSSION

A. AVNIR-2 and Pauli RGB Image Interpretation

The AVNIR-2 image of the Badrinath region and the adjoining Tibetan region of May 6, 2007 is shown in Fig. 5(a). Some part of this image is covered by cloud. Snow and nonsnow areas can be visually interpreted. The delineation of snow-cover and nonsnow-cover areas can be achieved on the optical image with the aid of the higher reflectance behavior of snow compared to other surface features including the glacier ice. However, it is difficult to separate clouds from snow without using a shortwave infrared (SWIR) band, which is not available in AVNIR-2 data but partly possible to recognize as snow-covered based on the associated pattern of glaciers shape in addition to the higher reflectance in AVNIR-2 image over Badrinath region. This interpretation helps in assigning the training sample for the supervised classification of ALOS–PALSAR data. However, before assigning the training samples to the supervised classifier, these samples were confirmed based on the advanced wide-field sensor (AWiFS) observation of the Indian Remote Sensing Satellite (IRS-P6) on May 10, 2007 with a spatial resolution of 56 m and four spectral bands (Green, Red, NIR, and SWIR). AWiFS image

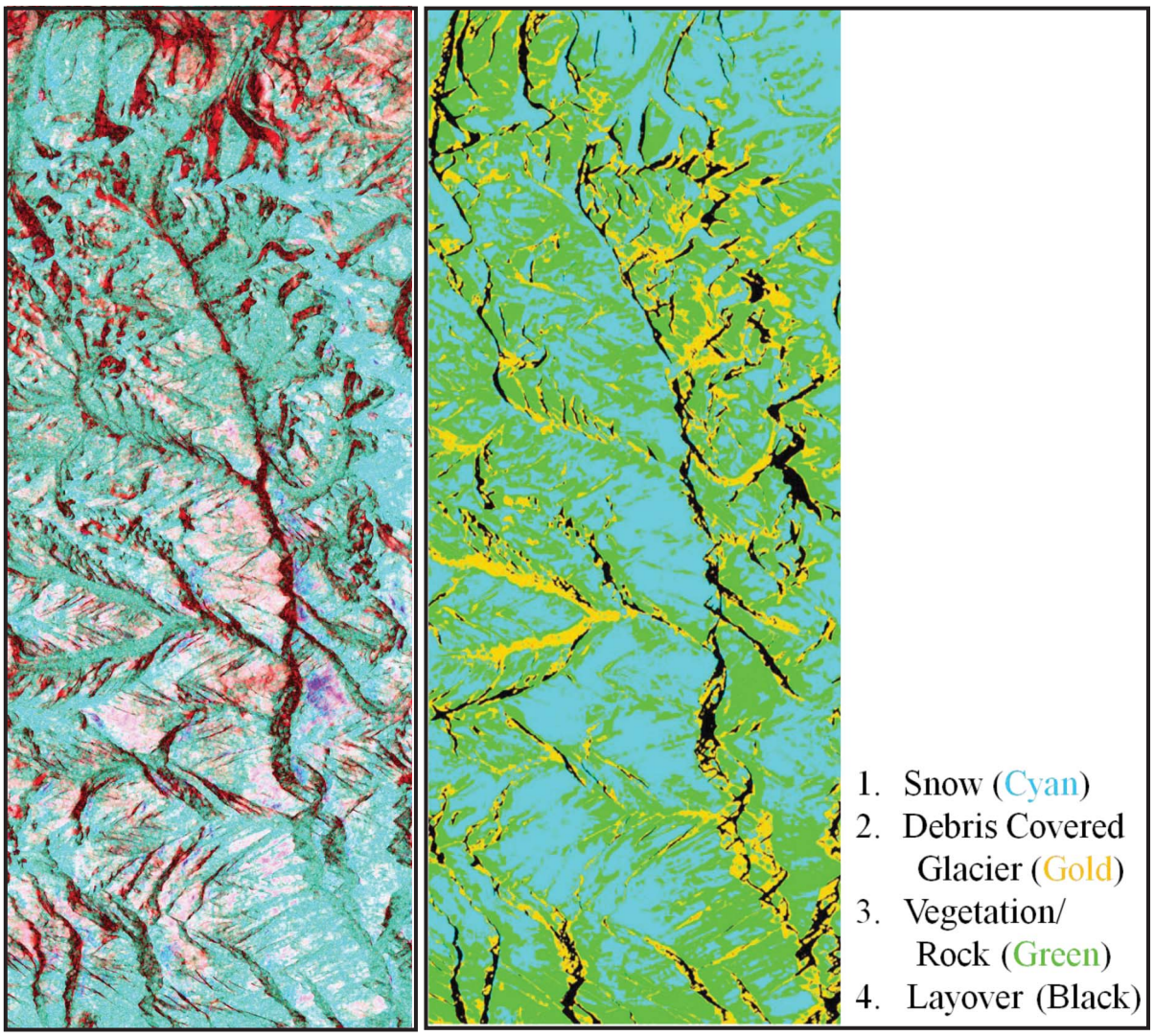

(a) (b)

Fig. 12. (a) $H/A/\bar{\alpha}$ (H-Green; A-Red; $\bar{\alpha}$-Blue) color combination image. (b) Wishart-supervised classified image.

of May 10, 2007 is shown in Fig. 5(b). Moreover, we have taken cloud-free images of AVNIR-2 for validation purpose of proposed methods as discussed in the next Section V.

Fig. 6(a) shows the standard Pauli color composite ALOS–PALSAR image of May 12, 2007. The Pauli RGB color-coding provides information about single-scattering (snow-cover area over glacier and nonglacier area), double-bounce (dihedral features), and volume-scattering (vegetation) of this study area. In the Pauli RGB of the ALOS–PALSAR image of the Satopanth glacier (Badrinath), most of the area [Fig. 6(a)] is in blue to deep-blue color due to single-scattering from the snow-cover over the glacier area (accumulation zone) and nonglacier area. The light-green to green color shows the vegetation (volume-scattering) area. Red color represents settlements exhibiting double-bounce or dihedral-scattering mechanism. The light-yellowish to white patches are layover effects due to high topography and low incident angle. The debris-covered glacier (ablation), denoted as debris-covered glacier (DCG), is shown in yellowish green color.

B. ALOS–PALSAR Backscatter Response

Fig. 6(b) shows the color composite image of backscattering coefficients (σ^0). Profiles have been drawn on σ^0 images of PALSAR for different scattering scenarios. Fig. 7 shows the backscatter profile of HH, HV, VH, and VV polarization channels for such different scattering scenes. The DCG profiles show high backscatter as compared to the snow-covered glacier. The ablation area of the glacier is highly crevassed and covered with moraine and debris material, which constitutes a very rough surface and returns back most of the SAR signal. Low-backscattering domains are seen on the smooth snow-covered glacier area. The main causes of the low backscatter over the snow area as compared to the DCG and vegetation are due to the wet snow conditions for which the attenuation increases by the snow-covered domain, whereas the smooth snow-covered glacier surface constitutes a specular reflector and does not reflect much energy back to the SAR sensor as in case of DCG and vegetation areas.

TABLE V
CONFUSION MATRIX FOR WISHART-SUPERVISED CLASSIFIED 4 CLASSES IN PALSAR IMAGE

Classified Sample	User-Defined Sample				
	Vegetation/Rock	DCG	Snow	Layover	Row Sum
Vegetation/Rock	1108	4	0	5	1117
DCG	0	1125	0	21	1146
Snow	1	0	1104	0	1105
Layover	0	61	0	1079	1140
Column Sum	1109	1190	1104	1105	4508
User's Accuracy (%)	99.19	98.17	99.91	94.65	Overall accuracy = 97.95%
Producer's Accuracy (%)	99.90	94.14	100	97.65	

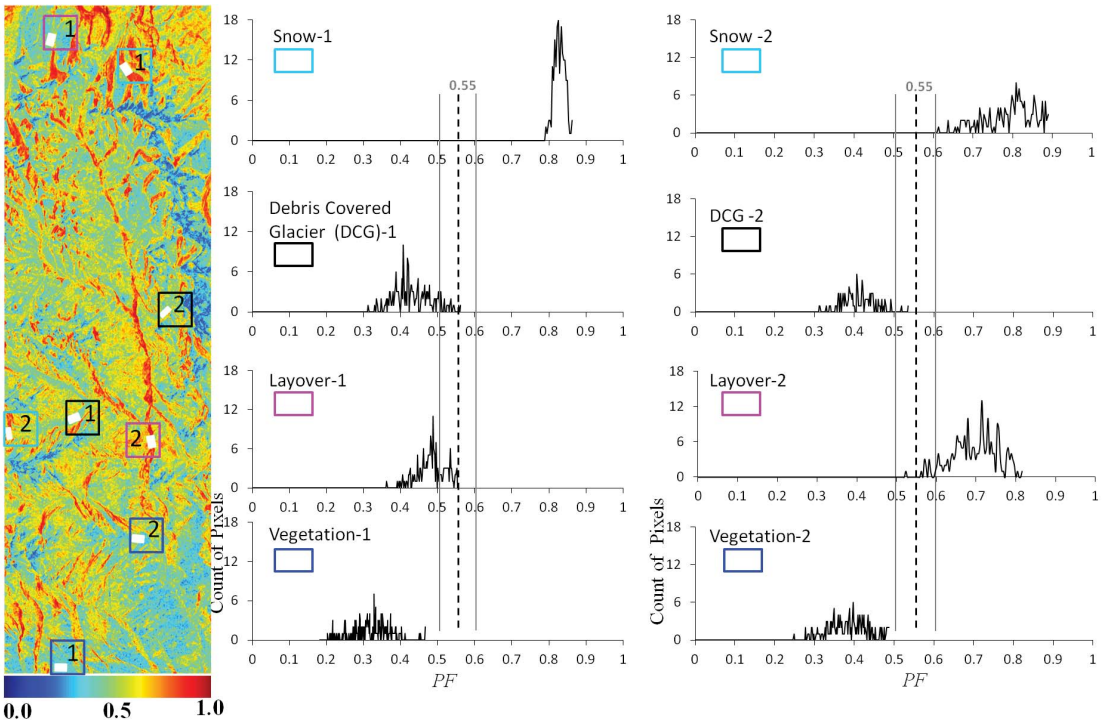

Fig. 13. PF image (left) and histograms PF of different class (white boxes on the left image with corresponding class's rims).

It is well known that L-band microwave signals penetrate through the dry snowpack with a negligible volume backscatter from snow. However, if the snowpack is wet, the situation changes markedly. If the moisture exceeds 1%, the L-band-frequency scatter suffers from attenuation in snowpack, while reflection or backscatter from snowpack becomes stronger [7]. The snow profile in Fig. 7 shows that the copolarization backscatter (HH and VV) responses are nearly 10 times larger than the cross-polarization backscatter (HV or VH) responses.

C. Yamaguchi Four-Component Scattering Power Decomposition Responses in Snow Areas

The physical interpretation of the four-component decomposition false-color composite FCC image over snow-covered areas is presented in [37], based on the fully polarimetric ALOS–PALSAR measurements. The HV component contributes to the volume scattering in the four-component scattering power decomposition scheme.

The HV component from snow is generated by multiple scattering in the media. The volume scattering increases with snow-grain size and internal layering, and with the amount of snow, when the wavelengths are close to the grain size in a snowpack according to Mie scattering theory. The Mie scattering predominates when the particles causing the scattering are larger than the wavelengths of radar in contact with them. However, the Mie scattering does not apply for wet snowpack in the L-band, where the wavelength is much larger than the snow particles. Therefore, it was observed that the volume scattering power response is lower than the surface scattering power responses from snowpack as a result of decomposition scheme [37]. Generally, the surface scattering is predominant in the total backscatter at small angles of incidence from the snow surface, and the volume scattering becomes predominant

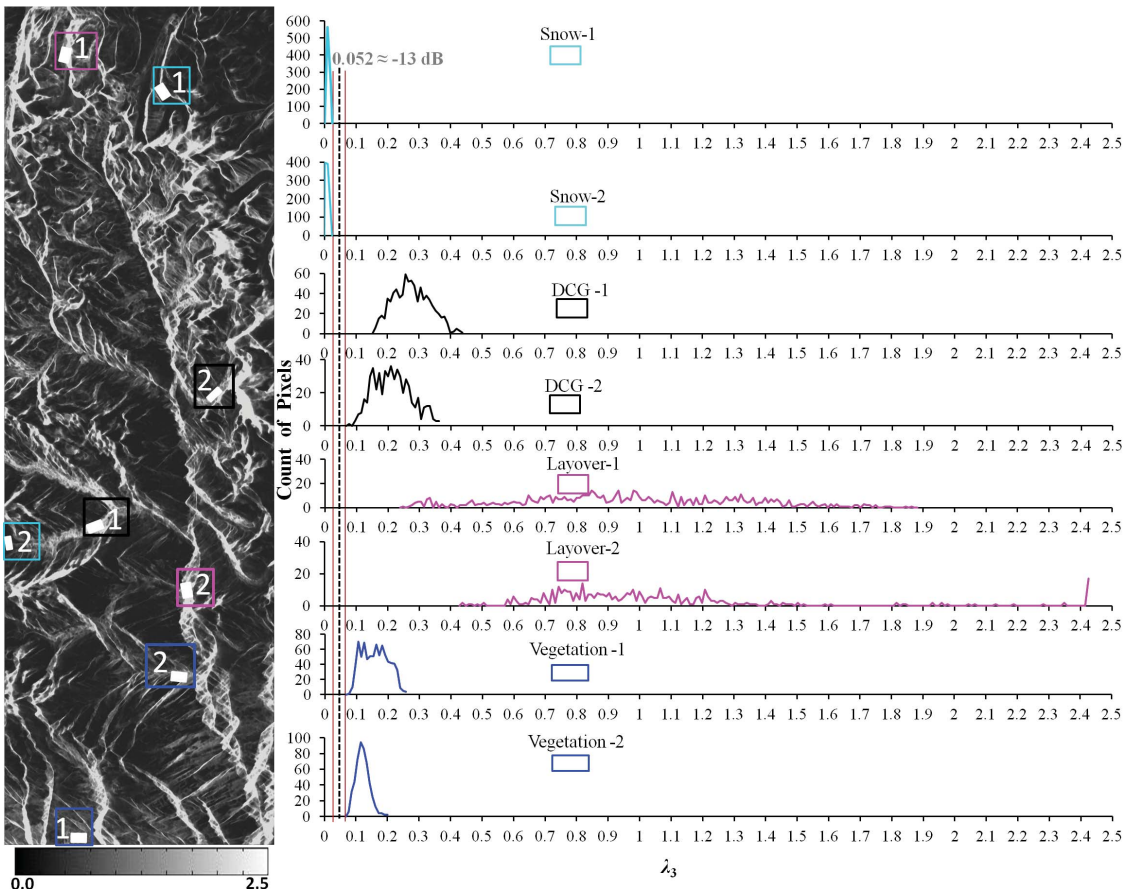

Fig. 14. λ_3 image (left) and histograms of λ_3 for various inherent scatterer types (white boxes on left image with corresponding class's rims).

at higher incident angles [1]. In addition, it was observed in [7] that the surface scattering over the snow-covered areas increases with snow volume, while the volume scattering remains small as compared to the surface scattering. These are the reasons why the surface scattering becomes dominant in the decomposition results in a snow-covered area as compared to the DCG and vegetation areas.

The evidence has been presented in Fig. 8, where a surface scattering from snow is clearly displayed. The polarimetric data set over the Gangotri glacier region was acquired with L-band PALSAR quad polarization mode at 21.5° of incident angle on June 06, 2010. The land cover includes snow, DCG domains, rocks, etc., (Fig. 8). ALOS–AVNIR-2 data (May 25, 2010) are used to interpret the glacier area. The comparison of the visual interpretation can be done for decomposition images with the cloud-free AVNIR-2 image in Fig. 8(b). The ablation area of the glacier is highly crevassed and covered with moraine and debris materials that create high-volume scattering power in the ablation area due to multiple-scattering phenomenons. This area appears green in the decomposition FCC image. The snowpack is wet during the melting phase in June. It can be seen from Fig. 8(b) that approximately half of the seasonal snowpack cover has been melting from the main glacier body. The wet snowpack represents blue color in the decomposition image because the surface scattering is dominant.

TABLE VI
λ_3 HISTOGRAM STATISTICS FOR VARIOUS FEATURES IN GLACIATED TERRAIN

	Min.	Max.	Mean	Median	Mode	Std. Dev.
Snow-1	0.010	0.029	0.017	0.010	0.010	0.002
Snow-2	0.000	0.024	0.009	0.000	0.000	0.002
DCG-1	0.162	0.437	0.282	0.277	0.257	0.058
DCG-2	0.076	0.362	0.219	0.209	0.209	0.058
Vegetation-1	0.076	0.257	0.155	0.152	0.095	0.041
Vegetation-2	0.076	0.200	0.126	0.115	0.115	0.022
Layover-1	0.238	1.882	0.971	0.937	0.837	0.348
Layover-2	0.437	2.424	1.044	0.951	2.424	0.404

In addition, blue dominates in a snow-free smooth bare surface [37]. In case some parts of snow-free areas are surface-scattering dominated, that situation can be problematic for the snowpack discrimination by using radar remote sensing at L-band. This may also appear at C-band [38] such as for the Tibetan plateau (smooth and flat terrain) region of the Himalayas. However, Himalayan glaciers on the Indian side are covered by debris that aids to determine the snow-cover at lower altitudes. This advantage makes L-band fully polarimetric radar sensing useful for the snow mapping. Rott *et al.* [29] derived the wet-snow signatures at C- and L-bands, and they

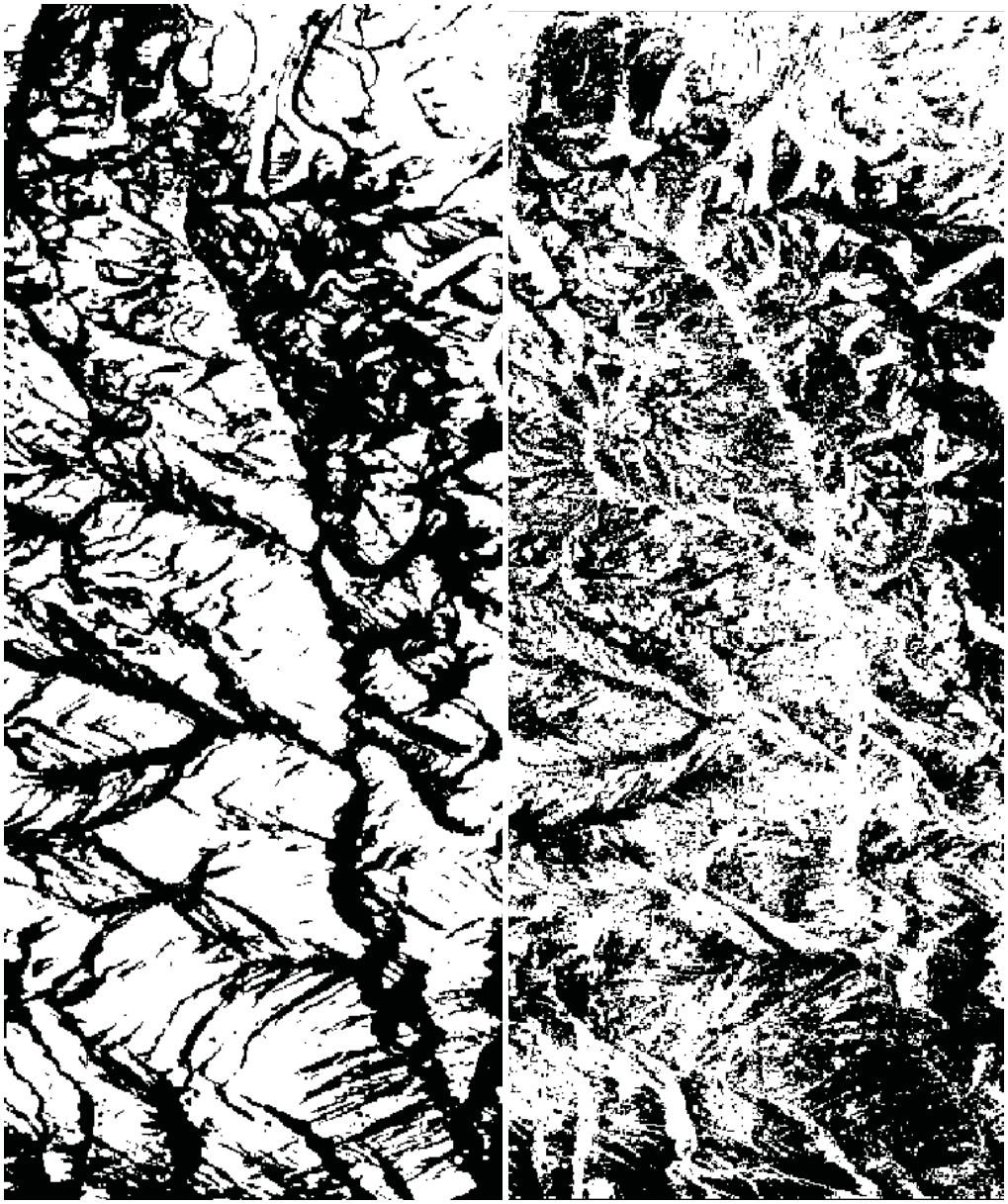

(a) (b)

Fig. 15. Binary images of (a) λ_3 (white < 0.052 and black ≥ 0.052) and (b) PF (white ≥ 0.55 and black < 0.55).

found very similar results. Longepe *et al.* [17] also found the effect of snowpack on polarimetric signatures at L-band. L-band SAR observations are sensitive to the snow-moisture variation and DCG domains, and provide useful information concerning the variation in its physical state. Therefore, the L-band fully polarimetric quad polarization radar is expected to play an important role in snow mapping in the Himalayan-glaciated terrain. However, improved comparisons for L-band and C-band versus S-band PolSAR image-data takes are desired and would be essential.

D. Single-Polarization and Multipolarization Repeat Passes Method for Snow-Cover Discrimination

ENVISAT–ASAR [Fig. 9(a)] and ALOS–PALSAR [Fig. 9(b)–(f)] derived snow-cover maps have been prepared. In this paper, a repeat-pass ratio method is used to separate snow from other natural and man-made scattering mechanisms for the backscatter ratio images. Based on the signature studies, field observations and comparison with optical data, a threshold -2 dB has been found to be appropriate by Rao *et al.* [12] for the ASAR backscatter ratio images over the Himalayan region using VV or HH scattering matrix components. With the available data sets of ENVISAT ASAR (May 19 and Nov. 10, 2007) and ALOS–PALSAR (May 12 and Nov. 27, 2007) ratio images have been generated as shown in Fig. 9, for which the November image was taken as reference. The ratio image enables snow change detection between May and Nov. 2007. The ratio between May and November images with threshold -2 dB for ENVISAT–ASAR and -1 dB for ALOS–PALSAR

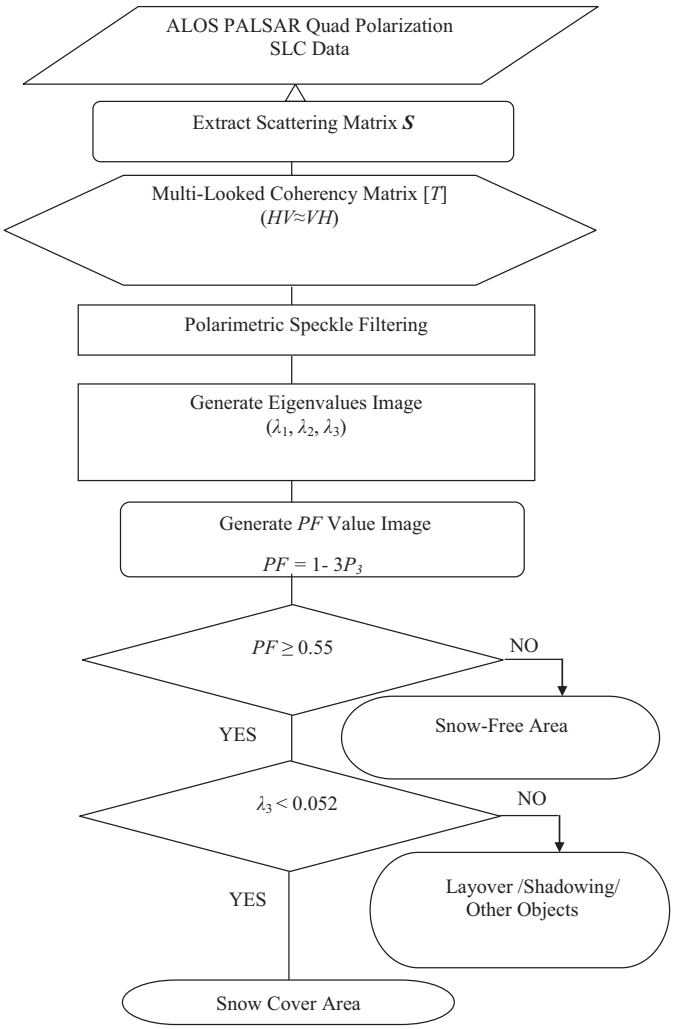

Fig. 16. Methodology flow chart of PF-based proposed method development.

provides the snow cover images. The resultant images of snow cover are shown in Fig. 9(a)–(f).

Due to melting of snow in May, the top layer of snow becomes wet and gives less backscattering as compared to that of the November image. From the classified images [Fig. 9(a)–(d)], it has been found that snow-covered areas at the accumulation region of the glacier on the right side of the image were classified as snow-free areas. Snow-covered areas are shown in cyan color. These classified SAR images are compared with the AVNIR-2 optical data of May 6, 2007 (Fig. 5). For multitemporal segmentation using snow-covered and reference images of different dates, various combinations of polarizations are explored and found that all combinations of backscatter power ratio with the same type of polarization scattering components such as HH/HH, VV/VV, and HV/HV are not suitable for the snow-cover mapping. In the case of repeat-pass ratio images, it is possible to use different type of polarization scattering components combinations such as HH/VV and HH/HV, in addition to the same type of polarization-scattering components combinations for extracting information about the wet snow-cover. But different type of polarization-scattering components' combination ratio images [Fig. 9(e)–(f)] are constrained by topographic distortion. Hence, it is important to create layover masks and shadowing masks for blocking distorted areas in the SAR images.

In this section, it has been seen that intermediate frequency L-band SAR data with single- and multipolarization combination of repeat passes do not properly discriminate the snow-cover (Table III). Snow discrimination problems of ratio techniques using multitemporal C-band and L-band SAR data in comparison of optical data (Fig. 5) are clearly indicated in Fig. 9. The accumulation area of the glacier in the optical (ALSO–AVNIR-2, Fig. 5) images is covered by snow, whereas snow maps derived on the basis of the ratio techniques using repeat-pass VV-polarization data of ENVISAT–ASAR [Fig. 9(a)] and ALOS–PALSAR [Fig. 9(b)] show snow-free areas.

E. Multipolarization Single-Pass Method for Snow-Cover Discrimination

Fig. 10 shows the histograms of the sigma naught ratio (HV/HH) image for snow, vegetation, DCG and snow with various DCG classes. Based on this plot, a threshold value 0.2 (≈ -7 dB) is determined to discriminate snow-cover from other scattering mechanisms. This investigation shows that the backscattering ratios of cross-polarized (VH) versus copolarized (VV) and cross-polarized (HV) versus copolarized (HH) are more suitable than other ratio combinations (Fig. 11). There is a need for topographic information to mask out the layover/shadowing regions. The HH/VV ratio image is inefficient for the snow discrimination (Fig. 11). HH/VV ratio enhances the double-bounce information from vegetation, and rocks in the study area; hence, it is difficult to discriminate snow occurring in association with these particular double-bounce scattering mechanisms.

Snow-free areas appear rough as compared to snow-covered areas in cross versus copolarization ratio images. Rough surface generates multiple scattering. Due to multiple scattering, the cross versus copolarization ratio provides high values over snow-free areas and low values over snow-covered areas. But the appearance of snow-covered and snow-free areas in co- versus cross-polarization ratios are opposite. Hence, these images of snow-covered areas show high values.

The accuracies for backscattering ratios of cross-polarized versus copolarized are analyzed and are shown in Table IV.

F. Decomposition Model for Snow-Cover Discrimination/Classification

The $H/A/\bar{\alpha}$ decomposition scheme is applied to L-band PALSAR data of May 12, 2007 over the Badrinath region where the land cover includes snow, vegetation, and glacier (Fig. 5). The $H/A/\bar{\alpha}$ false color composite image is presented in Fig. 12(a).

With the help of AVNIR-2 and AWiFS images, the training samples are selected for the field information gathering and for the Survey of India topography map. The supervised Wishart-classification technique was implemented for the coherency

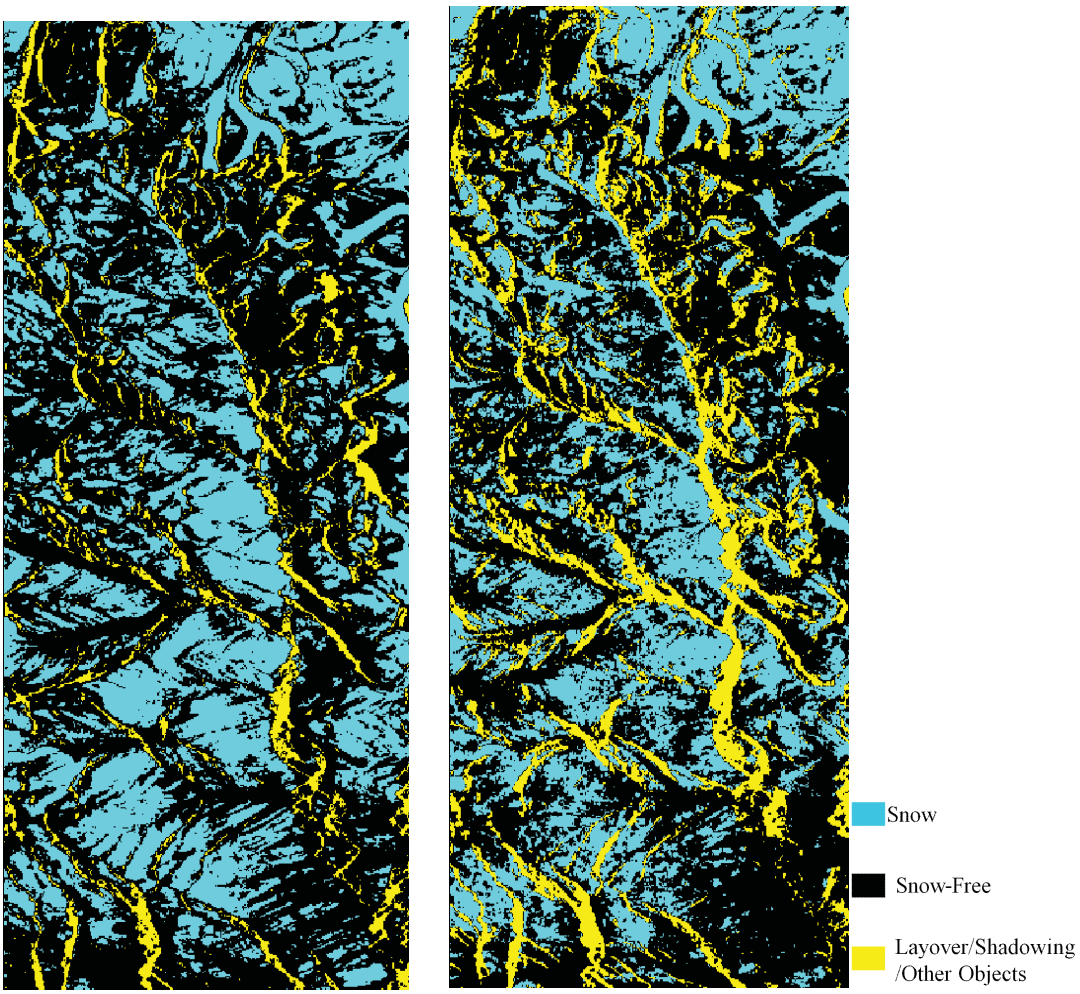

Fig. 17. (a) Total snow-cover map based on Fig. 12(b). (b) Proposed method-based snow-cover map.

TABLE VII
ACCURACY OF SNOW AND NONSNOW DISCRIMINATION BASED ON PF METHOD PERFORMANCE

User-Defined Sample	Classified Sample		
	Layover/Shadowing/ Other Objects (%)	Snow-Free (%)	Snow (%)
Layover/Shadowing/ Other Objects	91.02	8.98	0
Snow-Free (%)	1.96	97.95	0.09
Snow (%)	1.67	0.65	97.68
	Overall Accuracy = 95.44%		

matrix. The training sets for the snow-cover class and other classes have been allotted on the basis of visually comparing $H/A/\bar{\alpha}$ color-combination image with AVNIR-2 snow-cover image. Based on this allotment, ALOS–PALSAR data have been classified into four major classes including snow-covered, nonsnow-covered and layover, etc., [Fig. 12(b)]. The overall accuracy of classification is 97.95%. It is clear from Table V that the snow class has slightly higher user accuracy as compared to other classes.

G. PF for Snow-Cover Discrimination

The PF values have been calculated using (10). The PF values of the copolarization for snow, vegetation, and DCG features are 0.85, 0.59, and 0.33, respectively, and of the cross-polarization are 0.93, 0.49, and 0.51, respectively. These values are represented for single pixels of multilooked and speckle-filtered images. The PF images by using (11) have also been generated. The PF images (Fig. 13) also display a high PF value range for the snow-cover as compared to other scattering scenarios. Due to very-high PF values of snow, it is possible to distinctly delineate snow from other scatterers [18], [39].

In Fig. 13, histograms are plotted for various classes of PF values. It is seen from histograms and PF images, that the snow class can be discriminated by using the PF value but that the PF value of layover areas overlapped with PF values of snow-covered areas.

H. PF Method for Snow Discrimination

It was found in Fig. 13 that the snow-covered areas possess high PF values compared to other areas. This remarkable feature can be used for discriminating snow-covered from other areas. However, Fig. 13 also shows high PF values in snow-

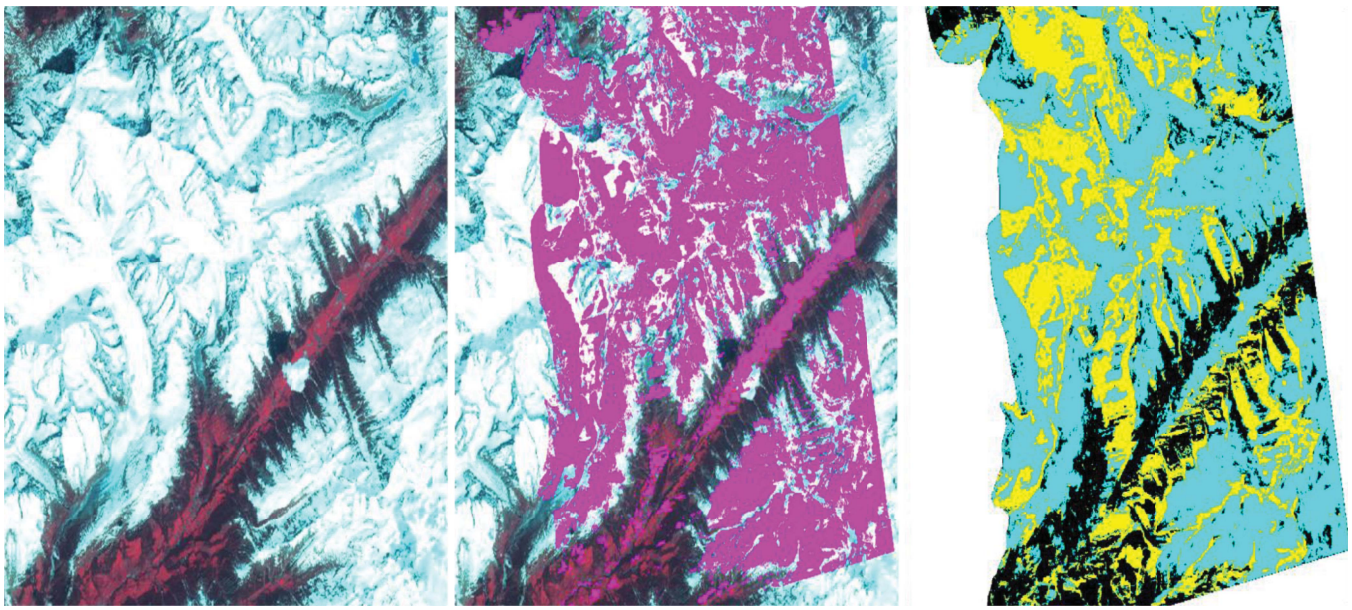

(a) (b) (c)

Fig. 18. (a) AVNIR-2 RGB of May 24, 2009 with < 2% cloud-cover over the Agassiz Horn-glaciated region in the Bernese Alps of Switzerland. (b) Proposed method-based derived snow-cover (in magenta) is overlaid to AVNIR-2 RGB to check the capability of PALSAR data for snow detection. (c) Snow-cover map derived from PF-based proposed method: snow (in cyan), layover/shadowing/other objects (in yellow), and snow-free (in black).

free areas at the lower central part of the image, where layover effects due to the high topography of the Himalayas exist. Hence, it is necessary to explore additional parameters to eliminate this ambiguity. In this investigation, the eigenvalue images of the coherency matrix have been used, in addition to the other parameters such as entropy (H), anisotropy (A), scattering mechanism angle ($\bar{\alpha}$), $(1-H)$, and $H(1-A)$, Lüneburg anisotropy, SERD, DERD, PPD, and copolarization coherence. These parameters have been analyzed to find out which one could serve to overcome the uncertainty in the results of snow discrimination obtained through PF in mountainous regions where layover and other scattering type of objects exist.

Entropy, $H(1-A)$, and Lüneburg anisotropy show low values over the snow-cover due to a pure single target and high values over the other distributed scattering regions (e.g., ablation area of DCGs and vegetation). On the other hand, polarimetric anisotropy and asymmetry exhibit high values over the snow-covered areas. All of these parameters are also capable of discriminating snow from other scattering mechanisms but do not have adequate range to suppress layover and shadowing topographically affected snow-free areas. The Shannon entropy [23] demonstrates the capability to suppress distorted areas in the classified image but it failed to discriminate snow from other scattering types in some parts of the images. Eigenvalues λ_1, λ_2, λ_3 of coherency matrix also show sufficient range for suppressing this unwanted area from the snow-cover areas and show very high value for the layover-affected area in the image. For selected portions of the image, which is affected by the topographic distortion, the first eigenvalue λ_1 is varying in a narrow range as compared to the second eigenvalue λ_2 and the third eigenvalue λ_3 ranges. Hence, the λ_1 is not able to discriminate snow from other inherent scattering mechanisms for the case of mountainous regions. The λ_2 range is mixing with the layover-affected areas in the upper part of the image. The λ_3 possesses a wide range, and hence it is possible to separate the affected area and other features. In other words, the λ_3 can be utilized for discrimination of snow-covered areas. Since the λ_3 is a measure of randomness of scattering mechanism [40], [41], use of the λ_3 certainly has some merit in the practical sense. For highly polarized scattering from the wet snow, the λ_3 will be low since most of the polarimetric information will be held within the first and second eigenvalues. When scattering becomes more random, in the presence of vegetation or debris covered glaciers, the λ_3 will be stronger. The interesting point comes with the layover discrimination; as layover is a highly random process, it generates higher values of the λ_3. Hence, the λ_3 has been used to remove the ambiguity in the discrimination of snow using the fractional polarization value. In order to find the appropriate threshold value of the λ_3 for discriminating snow-cover from other inherent scattering types, histograms are plotted in Fig. 14 for the snow, vegetation, DCG, and layover areas. Statistics of these histograms are shown in Table VI. After determining the appropriate threshold value 0.052 in Fig. 14, a binary image for the λ_3 has been generated. The binary image of the λ_3 together with the binary image of PF is shown in Fig. 15.

Finally, based on the above-discussed observations, a new alternative algorithm has been proposed for discriminating the snow from other pertinent scatterers, using the eigenvalues of the coherency matrix of the PolSAR data and the PF. The proposed algorithm flow chart for discriminating snow from other features is shown in Fig. 16. Fig. 17(b) represents binary maps showing the snow-covered, layover/shadowing/other objects and snow-free areas derived with the proposed method. It has been noticed that the snow-cover map, based on the proposed

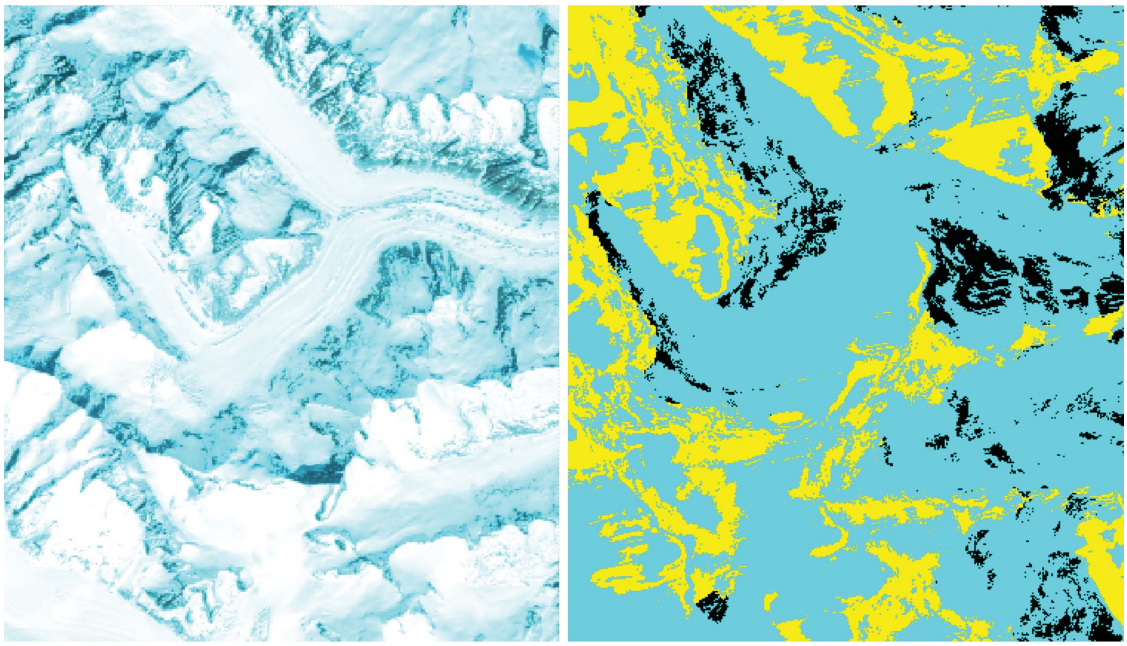

(a) (b)

Fig. 19. (a) Subset of ALOS–AVNIR-2 RGB of May 24, 2009 with < 2% cloud cover over the Agassiz Horn-glaciated region in the Bernese Alps of Switzerland. (b) Subset of derived snow-cover map from PF-based proposed method: snow (in cyan), layover/shadowing/other objects (in yellow), and snow-free (in black).

method, shows good agreement with the snow-cover maps obtained from implementation of the Wishart-supervised classifier [Fig. 17(a)].

An important aspect of this paper is to compare the snow-cover maps' performance obtained through the PF-based method and the Wishart-supervised classifier-derived snow-cover map performance. The performance of snow and nonsnow discrimination obtained through the PF-based method is given in Table VII. The PF-based proposed method provides a very close performance with that obtained from the Wishart-supervised classifier (see Table V). Since the performance of the proposed method is closely matching with the Wishart-supervised classifier, the proposed method, based on PF and the third eigenvalue of coherency matrix, has been shown to be reliable and robust in absence of training sets for the supervised classification methods.

V. Verification of Proposed Algorithm

To verify the correct implementation of this new scheme, the PF method has also been implemented to a pertinent section of the Bernese Alps of Switzerland. Obtained results with implementation of the fully polarimetric ALOS–PALSAR imagery using the proposed PF method are compared with one day-difference data of ALOS–AVNIR-2 [Fig. 18(a)]. For this purpose, the derived snow image is orthorectified and superimposed to AVNIR-2 image [Fig. 18(b)], and the derived snow-cover map is also shown in Fig. 18(c) with three classes: snow cover, layover/shadowing/other objects, and snow-free. The visual interpretation of Fig. 18 demonstrates clearly that, ALOS–PALSAR is less capable than the cloud-free AVNIR-2 data. The proposed method with L-band polarimetric SAR data classifies some snow-free areas as snow-covered when other Bragg type scattering objects, like agricultural fields, airport runways, water bodies, etc., are dominant. As mentioned before (Section IV-C), L-band polarimetric SAR may be useful for the mapping of the Indian Himalayan snow-cover because the Indian Himalayan glaciated terrain is covered by debris and agricultural fields are absent from the area.

For quantitative analysis, a subset of about a 88.34-square kilometer (km^2) area in the vicinity of the Agassiz Horn Mountain in the Bernese Alps of Switzerland has been chosen, as this area is less than 2% covered by cloud cover in some ALOS–AVNIR-2 images. However, the optical data and ALOS–PALSAR data have a temporal difference of one day. It can be safely assumed that there may not be any significant difference in the snow-cover extent, particularly in one day of early melting summer period. The PF-based proposed methods have been applied to fully polarimetric ALOS–PALSAR data of May 26, 2007. ALOS–AVNIR-2 image of May 24, 2009 covering Agassiz Horn mountainous region is shown in Fig. 19(a). Fig. 19(b) represents the proposed method-based classified total snow-cover area over Agassiz Horn-glaciated region. There is a difference of about 7.54% snow-cover area between AVNIR-2 and PF-based proposed method maps (Table VIII). The AVNIR-2 data discriminates more snow-covered area than from implementation of the PF-based proposed method. This may be attributed to the intrinsic character of the SAR sensor at L-band, which causes significant layover and shadowing effects due to the incident angle and topographic relief of the mountainous terrain.

Since the penetration depth at L-band can be over 1 m for wet snow with moisture range about 0.5%–1% by volume and density 0.3 g/cm^3, multiple scattering from underlying surface makes the discrimination difficult for shallow snow, and a S-band sensor could possibly improve the results.

TABLE VIII
AREA STATISTICS OF SNOW-COVERED REGION FOR FIG. 19

	Snow-Covered Area (%)	Layover/Shadowing/Other Objects Area (%)	Snow-Free Area (%)
Actual Snow-Cover (in AVNIR-2 Subset)	~ 100	-	~ 0
Detected Snow-Cover by Proposed Method	68.08	24.38	7.54

VI. PROPOSED METHOD'S ADVANTAGES AND DISADVANTAGES

In this section, we briefly discuss the advantages and disadvantages of the proposed method.

A. Advantages

1) Easy to implement on PolSAR data.
2) Training samples are not required.
3) It can be used without radiometric correction.

B. Disadvantages

Discrimination of snow from bare smooth surfaces and water bodies is still problematic. These feature conditions complicate matters particularly at L-band because of the inability of distinguishing dominant Bragg scattering from water bodies and smooth surfaces in general; then the problem may translate into the final snow image. L-band SAR (e.g., ALSO–PALSAR) may not able to detect the shallow-depth snow. In future work, the proposed method can be implemented by making use of C-band SAR data (e.g., RADARSAT-2), keeping in mind that fully polarimetric S-band PolSAR is required and may be the desired alternative between the L-band and C-band SAR implementations.

VII. CONCLUSION

Fully polarimetric data of snow-covered areas in the Indian Himalayan region were analyzed based on various component-scattering mechanism models and all known pertinent model results were compared. Single, dual, quad polarization L-band SAR data responses for the snow cover classification were also described in this paper. Co- and cross-polarized polarimetric signatures have been generated. The PF values have been calculated for assessing the capability of fully polarimetric ALOS–PALSAR data for the snow-cover discrimination.

It was found that single-polarization-based SAR measurements cannot discriminate the snow-cover over glacier regions and, furthermore, that SAR measurements for the dual polarizations are affected by topographic distortion and those were found to be prone to severe misinterpretation for discriminating the snow-covered areas from nonsnow-cover areas over the topography-distorted area. To overcome these problems, fully polarimetric PolSAR image data sets are required so that the new PF method can be introduced by integrating decomposition parameters for the snow discrimination from other inherent scattering types such as vegetation and debris prevalent in mountainous regions like the Indian Himalayas.

The PF value for snow is high as compared to other features, which indicates that the return signal is polarized. The user's accuracy in the confusion matrix (see Table V) of snow classes is higher than those of other classes. In addition, it has been observed that the less complex the PF-based method is, the better it maps closely to the supervised techniques viz. the Wishart-supervised classifier. It means that this new method of the PolSAR data based on the PF and the third eigenvalue of the coherency matrix is suitable for the snow-cover mapping in the absence of training samples or ground truth. The new alternative method has been verified for both fully polarimetric ALOS–PALSAR image data sets obtained over the test site of the Indian Himalayan region and that of the Agassiz Horn Mountain of the Bernese Alps in Switzerland, respectively.

This new method is robust and much simpler to implement as compared to the supervised methods like the Wishart-supervised classifier for the snow-cover mapping. Moreover, the PF-based method does not require any training sample and topographic information for snow discrimination from other scatterers inherent to these mountainous snow cover scenarios.

Due to the low incident angle and side-looking geometry of ALOS–PALSAR and the high topography of the Indian Himalayan terrain, the layover-affected areas are an inevitable image-distorting attribute to the image, and therefore, we cannot obtain full information of the inherent-scattering mechanisms. Furthermore, the ALOS–AVNIR-2-classified results in the case of cloud-free observations can be fused with ALOS–PALSAR-classified results to increase the classification accuracy and to reduce the effects of the layover and shadowing in the classified results. This paper can also be extended to the snowmelt runoff modeling and snow-avalanche risk assessment, which will be treated in separate ongoing studies.

ACKNOWLEDGMENT

The authors would like to thank Dr. Snehmani, Deputy Director, Snow and Avalanche Study Establishment, Chandigarh, India, for providing field condition. The authors would also like to thank Dr. W.-M. Boerner, Prof. Emeritus, University of Illinois at Chicago, Chicago, IL, USA, for corrections and suggestions to improve this paper.

REFERENCES

[1] F. T. Ulaby, R. K. Moore, and A. K. Fung, *Microwave Remote Sensing: Active and Passive, from Theory to Applications*. Reading, MA, USA: Addison-Wesley, 1986.

[2] M. Hallikainen, F. T. Ulaby, and M. Abdelrazik, "The dielectric properties of snow in the 3 to 37 GHz range," *IEEE Trans. Antennas Propag.*, vol. 34, no. 11, pp. 1329–1340, Nov. 1986.

[3] J. Shi and J. Dozier, "Estimation of snow water equivalence using SIR-C/X SAR. I. Inferring snow density and subsurface properties," *IEEE Trans. Geosci. Remote Sens.*, vol. 38, no. 6, pp. 2465–2474, Nov. 2000.

[4] F. T. Ulaby and W. H. Stiles, "The active and passive microwave response to snow parameters: 2. Water equivalent of dry snow," *J. Geophys. Res., Oceans*, vol. 85, no. C2, pp. 1045–1049, Jan. 1980.

[5] W. H. Stiles and F. T. Ulaby, "The active and passive microwave response to snow parameters: 1. Wetness," *J. Geophys. Res., Oceans*, vol. 85, no. C2, pp. 1037–1044, Jan. 1980.

[6] C. Mätzler and E. Schanda, "Snow mapping with active microwave sensors," *Int. J. Remote Sens.*, vol. 5, no. 2, pp. 409–422, Feb. 1984.

[7] T. Abe, Y. Yamaguchi, and M. Sengoku, "Experimental study of microwave transmission in snowpack," *IEEE Trans. Geosci. Remote Sens.*, vol. 28, no. 5, pp. 915–921, Sep. 1990.

[8] J. Shi, J. Dozier, and H. Rott, "Deriving snow liquid water content using C-band polarimetric SAR," in *Proc. Int. Geosci. Remote Sens. Symp.*, Aug. 1993, pp. 1038–1041.

[9] J. Shi and J. Dozier, "Inferring snow wetness using C-band data from SIR-C's polarimetric synthetic aperture radar," *IEEE Trans. Geosci. Remote Sens.*, vol. 33, no. 4, pp. 905–914, Jul. 1995.

[10] T. Nagler, "Methods and analysis of SAR data from ERS-1 and X-SAR for snow and glacier applications," Ph.D. dissertation, Inst. Meteorol. Geophys., Univ. Innsbruck, Innsbruck, Austria, Sep. 1996.

[11] J. T. Koskinen, J. T. Pulliainen, and M. T. Hallikainen, "The use of ERS-1 SAR data in snow melt monitoring," *IEEE Trans. Geosci. Remote Sens.*, vol. 35, no. 3, pp. 601–610, May 1997.

[12] Y. S. Rao, G. Venkataraman, and G. Singh, "ENVISAT-ASAR data analysis for snow cover mapping over Gangotri region," *Proc. SPIE*, vol. 6410, pp. 59–66, Dec. 2006.

[13] K. Luojust, J. T. Puliiainen, S. Metsamaki, and M. T. Hallikainen, "Accuracy assessment of SAR data based snow-covered area estimation method," *IEEE Trans. Geosci. Remote Sens.*, vol. 44, no. 2, pp. 277–287, Feb. 2006.

[14] J. Shi and J. Dozier, "Measurements of snow and glacier-covered areas with single polarization SAR," *Ann. Glaciol.*, vol. 17, pp. 72–76, Feb. 1993.

[15] G. Venkataraman, G. Singh, and V. Kumar, "Snow cover area monitoring using multitemporal TerraSAR-X data," in *Proc. 3rd TerraSAR-X Sci. Team Meeting*, 2008, pp. 1–7.

[16] A. Martini, "Télédétection d'un couvert neigeux en milieux alpins à partir de données SAR polarimétriques multi-fréquentielles et multi-temporelles," Ph.D. dissertation, Inst. d'Electron. et de Telecommun. de Rennes (IETR), Universite de Rennes 1, Rennes, France, 2005.

[17] N. Longepe, M. Shimada, S. Allain, and E. Pottier, "Capabilities of full-polarimetric PALSAR/ALOS for snow extent mapping," in *Proc. IEEE Int. Geosci. Remote Sens. Symp.*, vol. 4. Jul. 2008, pp. 1026–1029.

[18] G. Singh, "SAR polarimetry techniques for snow parameters estimation," Ph.D. dissertation, Centre Stud. Resour. Eng. (CSRE), Indian Inst. Technology Bombay, India, Sep. 2010.

[19] G. Singh and G. Venkataraman "Snow permittivity retrieval inversion algorithm for estimating snow wetness," *Geocarto Int.*, vol. 25, no. 3, pp. 187–212, Feb. 2010.

[20] V. S. Frost, A. S. Josephine, K. S. Holtzman, and C. Julian, "A model for radar images and its application to adaptive digital filtering of multiplicative noise," *IEEE Trans. Pattern Anal. Mach. Intell.*, vol. 4, no. 2, pp. 157–166, Mar. 1982.

[21] H. Rott and T. Nagler, "Snow and glacier investigations by ERS-1 SAR: First results," in *Proc. 1st ERS-1 Symp.*, Nov. 1992, pp. 577–582.

[22] "ALOS products, information ALOS PALSAR products for ADEN users reference," ESA, Paris, France, Tech. Rep. ALOS-GSEG-EOPG-TN-07-0001, 2007.

[23] J. S. Lee and E. Pottier, *Polarimetric Radar Imaging: From Basics to Application*. Boca Raton, FL, USA: CRC Press, 2009.

[24] M. Fily, J. P. Dedieu, and S. Surdyk, "A SAR image study of a snow-covered area in the French Alps," *Remote Sens. Environ.*, vol. 51, no. 2, pp. 253–262, Feb. 1995.

[25] A. Kaab, "Combination of SRTM3 and repeat ASTER data for deriving alpine glacier flow velocities in the Bhutan Himalaya," *Remote Sens. Environ.*, vol. 94, no. 4, pp. 463–474, Feb. 2005.

[26] P. Reinartz, R. Müller, P. Schwind, S. Suri, and R. Bamler, "Orthorectification of VHR optical satellite data exploiting the geometric accuracy of TerraSAR-X data," *ISPRS J. Photogram. Remote Sens.*, vol. 66, no. 1, pp. 124–132, Jan. 2011.

[27] J. Shi, J. Dozier, and H. Rott, "Snow mapping in alpine regions with synthetic aperture radar," *IEEE Trans. Geosci. Remote Sens.*, vol. 32, no. 1, pp. 152–158, Jan. 1994.

[28] J. Shi and J. Dozier, "Mapping of seasonal snow with SIR C/X-SAR in mountainous areas," *Remote Sens. Environ.*, vol. 59, no. 2, pp. 294–307, Feb. 1997.

[29] H. Rott, R. Davis, and J. Dozier, "Polarimetric and multifrequency SAR signatures of wet snow," in *Proc. Int. Geosci. Remote Sens. Symp.*, vol. 2. May 1992, pp. 1658–1660.

[30] S. R. Cloude and E. Pottier, "An entropy based classification scheme for land applications of polarimetric SAR," *IEEE Trans. Geosci. Remote Sens.*, vol. 35, no. 1, pp. 68–78, Jan. 1997.

[31] Y. Yamaguchi, Y. Yajima, and H. Yamada, "A four-component decomposition of POLSAR images based on the coherency matrix," *IEEE Geosci. Remote Sens. Lett.*, vol. 3, no. 3, pp. 292–296, Jul. 2006.

[32] Y. Yamaguchi, "Decomposition of PALSAR polarimetric data on Chuetsu area in Niigata prefecture," in *Proc. 1st ALOS PI Symp.*, 2007, pp.1–6.

[33] J. van Zyl, H. A. Zebker, and C. Elachi, "Imaging radar polarization signatures: Theory and observation," *Radio Sci.*, vol. 22, no. 4, pp. 529–543, Jan. 1987.

[34] T. L. Ainsworth, S. R. Cloude, and J. S. Lee, "Eigenvector analysis of polarimetric SAR data," in *Proc. IEEE Int. Geosci. Remote Sens. Symp.*, vol. 1. Nov. 2002, pp. 626–628.

[35] E. Lüneburg, "Foundations of the mathematical theory of polarimetry," EML Consultants Ltd., Colombo, Sri Lanka, Tech. Rep. N00014-00-M-0152, 2001.

[36] S. Allain, L. Ferro-Famil, and E. Pottier, "A polarimetric classification from PolSAR data using SERD/DERD parameters," in *Proc. 6th Eur. Conf. Synth. Aperture*, May 2006, p. 4.

[37] Y. Yamaguchi, W.-M. Boerner, R. Sato, and H. Yamada, "ALOS–PALSAR Quad. Pol. Imagesand their applications," in *Proc. 2nd Asian-Pacific Conf. Synth. Aperture Radar*, Oct. 2009, pp. 755–758.

[38] L. Huang, Z. Li, S.-S. Tian, Q. Chen, J.-L. Liu, and R. Zhang, "Classification and snow line detection for glacial area using polarimetric SAR image," *Remote Sens. Environ.*, vol. 115, no. 7, pp. 1721–1732, Jul. 2011.

[39] G. Singh, G. Venkataraman, V. Kumar, Y. S. Rao, and Snehmani, "The H/A/Alpha polarimetric decomposition theorem and complex wishart distribution for snow cover monitoring," in *Proc. IEEE Int. Geosci. Remote Sens. Symp.*, vol. 4. Jul. 2008, pp. 1081–1084.

[40] J. van Zyl and Y. Kim, *Synthetic Aperture Radar Polarimetric*. New York, USA: Wiley, 2011.

[41] I. Hajnsek, E. Pottier, and S. R. Cloude, "Inversion of surface parameters from polarimetric SAR," *IEEE Trans. Geosci. Remote Sens.*, vol. 41, no. 4, pp. 727–744, Apr. 2003.

Gulab Singh (S'09–M'10) was born in Saloonii-Sarsawa-Saharanpur, India. in 1976. He received the B.Sc. and M.Sc. degrees in physics from Choudhary Charan Singh University (formerly Meerut University), Meerut, India, in 1998 and 2000, respectively, the M.Tech. degree in remote sensing from the Birla Institute of Technology, Ranchi, India, and the Ph.D. degree from the Indian Institute of Technology Bombay, Mumbai, India, in 2005 and 2011, respectively.

He has honored with the *Award for Excellence in Thesis Work* for his outstanding research contributions from Indian Institute of Technology Bombay, in August 2011. From 2002 to 2003, he was a Physics Lecturer with Janta Inter College Jhabiran, Saharanpur, India. From 2005 to 2007, he was a Senior Research Fellow with the Centre of Studies in Resources Engineering, Indian Institute of Technology Bombay, where he was involved in several research projects related to POL-SAR and In-SAR data analysis for snow and ice parameters retrieval. Since 2010, he has been the Post Doctoral Fellow with the Graduate School of Science and Technology, Niigata University, Niigata, Japan. His current research interests include SAR data analysis, SAR polarimetry and SAR interferometry techniques development for earth, and lunar surface parameters estimation.

Gopalan Venkataraman received the M.Sc. and Ph.D. degrees in applied geology from the Indian Institute of Technology Bombay, Mumbai, India, in 1971 and 1976, respectively.

He has been with the Centre of Studies in Resources Engineering, Indian Institute of Technology Bombay, India since 1976. He has been carrying out research in remote sensing and GIS applications to geological and environmental problems. He visited ITC (Enschede and Delft), The Netherlands, on a scientific exchange program for research in the area of Spatial modeling for mineral experience in 1989. He has also carried out many research projects in the field of remote sensing applications to the mineral exploration, environmental impact of mining and desertification for ISRO, DST, Ministry of Environmental and Forest. For the last 15 years, he has been emphasizing on research relating to snow and glaciers studies particularly involving active and passive microwave remote sensing data. He is also involved in some international projects with ESA, DLR, and JAXA. Through these projects he is able to carry out many research projects for DST and DRDO using ENVISAT ASAR, TerraSAR-X, and ALOS PALSAR data products. His recent research projects include studies relating to glacier facies mapping, snow pack characteristics, and movement of glaciers using interferometry techniques. He has authored 50 international publications in referred journals and conferences proceedings. Currently, he is actively involved in the M.Tech. and Ph.D. academic program of the centre.

Yoshio Yamaguchi (M'83–SM'94–F'02) received the B.E. degree in electronics engineering from Niigata University, Niigata, Japan, in 1976, and the M.E. and Dr.Eng. degrees from the Tokyo Institute of Technology, Tokyo, Japan, in 1978 and 1983, respectively.

He joined the Faculty of Engineering, Niigata University, in 1978. From 1988 to 1989, he was a Research Associate with the University of Illinois at Chicago, Chicago, IL, USA. He is currently with the Graduate School of Science and Technology, Niigata University. His current research interests include radar polarimetry, microwave sensing, and imaging. Dr. Yamaguchi has served as the Chair of the IEEE Geoscience & Remote Sensing Society (GRSS) Japan Chapter (2002–2003), the Chair of the International Union of Radio Science Commision F Japanese Committee (URSI-F) Japan (2006–2011), an Associate Editor for Asian affairs of GRSS Newsletter (2003–2007), and the Technical Program Committee (TPC) Co-Chair of the 2011 IEEE International Geoscience and Remote Sensing Symposium (IGARSS). He is a Fellow of the Institute of Electronics, Information and Communication Engineers (IEICE), Japan. He was recipient of the 2008 IEEE GRSS Education Award.

Sang-Eun Park (S'05–M'07) received the B.S. and M.S. degrees in geophysics and the Ph.D. degree in radar remote sensing and geophysics from the Seoul National University, Seoul, Korea, in 2000, 2002, and 2007 respectively.

He was a Post-Doctoral Fellow on radar polarimetry with the Radar Polarimetry Remote Sensing Group, University of Rennes 1, Rennes, France, from 2007 to 2009. From October 2009 to January 2010, he was a Project Scientist with the Institute of Photogrammetry and Remote Sensing, Vienna University of Technology, Vienna, Austria. He is currently an Assistant Professor with the Graduate School of Science and Technology at Niigata University, Japan. His current research interests include polarimetric SAR classification, forward and inverse modeling of microwave vegetation and surface backscattering, and investigation of multi-source data integration methodology.